Earth Analogs in Reflected Light: Insights from Early Spectral Characterization in Unconstrained Orbits

Arnaud Salvador $\bigcirc^{1,2,3,4,5}$ and Tyler D. Robinson $\bigcirc^{1,2,3,4}$

¹Lunar & Planetary Laboratory, University of Arizona, Tucson, AZ 85721, USA
²Department of Astronomy and Planetary Science, Northern Arizona University, Flagstaff, AZ 86011, USA

³ Habitability, Atmospheres, and Biosignatures Laboratory, University of Arizona, Tucson, AZ 85721, USA

⁴ NASA Nexus for Exoplanet System Science Virtual Planetary Laboratory, University of Washington, Box 351580, Seattle, WA 98195,

 5 Institute of Space Research, German Aerospace Center (DLR), Rutherfordstr. 2, 12489 Berlin, Germany

Submitted to ApJ; Accepted October 21, 2025 - doi:10.3847/1538-4357/ae16a1

ABSTRACT

A next generation of space-based observatories aims to detect and characterize potentially Earthlike exoplanets around Sun-like stars using reflected light spectroscopy. However, it remains unclear how such direct imaging observations—limited in spectral coverage and signal-to-noise ratio (S/N) translate into constraints on atmospheric composition and habitability. Coronagraphs used for highcontrast imaging typically operate over narrow bandpasses, and exposure time limits can restrict data quality. To optimize observing strategies and instrument design, we use our atmospheric retrieval tool, rfast, to assess the performance of a Habitable Worlds Observatory-type mission across different spectral bandpasses ("Red", "Blue", "Visible", "NIR", and their combination) and S/N levels (10, 15, and 20; from moderate to moderate-high observation quality) in retrieving a wide range of 17 atmospheric, surface, bulk, and orbital parameters of a habitable Earth analog. We outline the observation requirements for each parameter and the detection capabilities of each case, within a novel scenario where spectral data are taken "early", prior to achieving orbit constraints (which may require repeat visits to a system). For coronagraph-restricted and NIR-only bandpasses, most of the limited retrievable information is already captured at S/N = 10, with little improvement at higher S/N. For broader spectral coverage, the quality and quantity of retrieved information improve with increasing S/N, but combining visible and NIR ranges provides the most comprehensive characterization, even at moderate S/N. To maximize returns, wider spectral coverage should be prioritized over improving S/N when spectral access is limited.

Keywords: Exoplanets (498) — Direct imaging (387) — Exoplanet atmospheres (487) — Astrobiology (74) — Biosignatures (2018) — Bayesian statistics (1900) — Habitable planets (695)

1. INTRODUCTION

With over 5900 confirmed exoplanets¹—more than a third of which are rocky—detecting and characterizing habitable worlds (i.e., where liquid water is stable at the planetary surface; Kasting et al. 1993; Kopparapu et al. 2013) has become a major goal for the next decade (National Academies of Sciences, Engineering, and Medicine 2021, 2022). Direct imaging and reflected light spectroscopy are promising methods for detailed characterization of exoplanetary atmospheres and surface conditions, which are critical for assessing the potential habitability of a world. However, such observations require starlight suppression techniques (e.g., coronagraphs or starshades) to achieve the necessary

Corresponding author: Arnaud Salvador arnaud.salvador@dlr.de

¹ https://exoplanetarchive.ipac.caltech.edu

< 10⁻¹⁰ planet-to-star flux contrast for direct imaging of Earth-like planets around Sun-like stars (orbiting at 1 au and observed in optical wavelengths; e.g., Guyon et al. 2006; Seager & Deming 2010). NASA's upcoming Nancy Grace Roman Space Telescope² will be a major milestone in space-based coronagraphy, demonstrating high-contrast imaging capabilities with unprecedented observations of nearby giant exoplanets (Bailey et al. 2018; Akeson et al. 2019; Mennesson et al. 2020; Kasdin et al. 2020; Mennesson et al. 2022). This mission will pave the way for the direct imaging of exo-Earths with NASA's proposed Habitable Worlds Observatory (HWO; building upon the earlier HabEx and LUVOIR mission concepts, e.g., Gaudi et al. 2018, 2020; Roberge & Moustakas 2018; The LUVOIR Team 2019).

To design exo-Earth direct imaging missions and assess the returns of proposed instruments and observing scenarios, atmospheric retrieval models are commonly used (e.g., Madhusudhan 2018; Fortney et al. 2021). These models infer the range of exoplanet properties that can explain either actual or synthetic observations and can thus assess how future instruments and observations will translate into constraints on these parameters.

Recent studies have focused on the characterization of gas and ice giants in reflected light including with the upcoming Roman Space Telescope (e.g., Marley et al. 2014; Lupu et al. 2016; Nayak et al. 2017; Carrión-González et al. 2020; Damiano & Hu 2020; Damiano et al. 2020; Carrión-González et al. 2021), as well as on Earth-twins imaging (e.g., Feng et al. 2018; Smith et al. 2020; Damiano & Hu 2022; Robinson & Salvador 2023; Hall et al. 2023; Susemiehl et al. 2023; Kofman et al. 2024). These efforts typically target the detectability of specific parameters such as habitability indicators and biosignature gases (e.g., Wang et al. 2018; Latouf et al. 2023a,b, 2024; Metz et al. 2024; Tokadjian et al. 2024; Currie & Meadows 2025) or the inference capabilities under specific observing scenarios (Damiano et al. 2023; Young et al. 2024; Salvador et al. 2024; Damiano et al. 2025). Parallel studies have explored habitable planet characterization using transmission spectroscopy (e.g., Benneke & Seager 2012; Greene et al. 2016; Min et al. 2020; Pidhorodetska et al. 2020; Gialluca et al. 2021; Currie et al. 2023; Meadows et al. 2023; Lustig-Yaeger et al. 2023), thermal emission (e.g., von Paris et al. 2013; Stevenson 2020; Lustig-Yaeger et al. 2021; Fujii & Matsuo 2021; Mandell et al. 2022; Konrad et al. 2022; Alei et al. 2022; Mettler et al. 2024), and potential synergies across different techniques and missions (e.g., Gilbert-Janizek et al. 2024; Alei et al. 2024).

However, a persistent challenge in atmospheric retrievals is the degeneracy between inferred parameters (e.g., Welbanks & Madhusudhan 2019; Barstow & Heng 2020; Novais et al. 2025): multiple combinations of parameters (e.g., cloud properties, planetary radius, surface albedo, phase angle, orbital distance) can produce similar spectra, making it difficult to disentangle their individual influences (e.g., Nayak et al. 2017; Wang et al. 2022; Salvador et al. 2024). Constraining certain parameters can help break degeneracies and enable/enhance the inference of correlated ones (e.g., constraining the orbital parameters allows to infer the planetary radius, which itself refines clouds optical depth and methane inferences; Nayak et al. 2017; Carrión-González et al. 2020, 2021; Salvador et al. 2024), but risks introducing artificial bias when only a limited number of parameters are inferred. A fully agnostic approach, where all relevant parameters remain unconstrained unless informed by existing data, is also essential for robust target identification during an initial blind-search phase before follow-up observations (e.g., The LUVOIR Team 2019), in a self-contained survey (e.g., Gaudi et al. 2020), or to assess the full capabilities of HWO in its different observing phases. This approach ensures that the analysis reflects the uncertainty inherent in exoplanet observations, where most parameters are unknown and need to be explored. To better reflect the complexity of actual observations and minimize potential biases, inverse modeling should not focus solely on habitability indicators but rather aim to retrieve as many spectrally relevant parameters as possible.

Furthermore, modeling efforts must contend with the generally detrimental effects of clouds and hazes. While hazes can possibly inform planetary composition and processes (e.g., Corrales et al. 2023), and clouds improve the detectability of atmospheric constituents in specific cases (e.g., Kelkar et al. 2025), they can mute absorption features of key atmospheric species (e.g., Fauchez et al. 2019; Komacek et al. 2020; Pidhorodetska et al. 2020; Barstow & Heng 2020; Kelkar et al. 2025). Broader wavelength coverage can mitigate the resulting degeneracies between gas abundances and cloud properties (e.g., Fauchez et al. 2019; Barstow & Heng 2020), but observing time limitations and instrumental constraints—such as the restricted bandpass of coronagraphs—reduce achievable S/N and spectral coverage. These observations may miss key spectral information, leading to biased retrievals of atmospheric composition and cloud properties (e.g., Mai & Line 2019; Kelkar et al. 2025). In addition, if the latter are not retrieved, fixed cloud parameterizations may become inconsistent with sampled atmospheric states, failing to capture their spectral effects and leading to unrealistic results. For example, if water vapor abundance is retrieved without accounting for

² https://roman.gsfc.nasa.gov

corresponding changes in water cloud parameterization (as considered in Damiano et al. 2023, 2025, which ensures physical consistency between water vapor and cloud formation), inconsistencies between the sampled values of water vapor and the spectral imprints of water clouds could bias the retrievals and compromise their validity. While Barstow (2020) demonstrated its moderate influence on the retrieved abundance of H₂O from transmission spectroscopy, this effect has not been investigated for reflected light observations and a broader range of retrieved parameters, which should further be addressed in a dedicated study.

Focusing on isolated parameters or narrow bandpasses can therefore bias retrieval analysis and fail to capture the broader challenges of exoplanet characterization under limited observational knowledge. Despite recent advances, it remains unclear how direct imaging observations—limited by spectral coverage and observational noise—translate into constraints on atmospheric composition and key indicators of habitability. A systematic comparison of retrieval performance across different spectral ranges, S/N levels, and a large number of unconstrained parameters is still lacking. A critical challenge is defining the most efficient observing strategies to robustly identify Earth analogs. One possible approach involves an initial large-scale survey using time-limited, lower S/N observations in a reduced bandpass focused on water vapor detection, followed by a more detailed characterization of the most promising candidates with full spectral capabilities (e.g., The LUVOIR Team 2019). In this scenario, it is essential to understand (1) what constraints can be obtained from reduced-bandpass, low (to high) S/N observations when most parameters are unknown, and (2) how these constraints inform or bias spectral interpretation. This work aims to fill this gap by systematically evaluating how spectral coverage (including coronagraph-restricted bandpasses) and S/N impact the identification of Earth-like habitable worlds. Specifically, we investigate how these factors influence the retrieval of atmospheric and bulk properties of an Earth analog observed in reflected light without prior determination of the orbit. In doing so, we aim to provide key insights that will help inform the design of future direct imaging missions, such as HWO, and optimize observing strategies to balance spectral completeness, observing time, and scientific yield. Section 2 describes our retrieval tool rfast—designed to explore high-dimensional parameter spaces efficiently

Section 2 describes our retrieval tool rfast—designed to explore high-dimensional parameter spaces efficiently without prohibitive computational costs (e.g., Robinson & Salvador 2023; Hall et al. 2023; Salvador et al. 2024)—as well as the inferred parameters and the observing scenarios considered. Section 3 presents our findings, followed by a discussion of their implications for future exo-Earth characterization with HWO in Section 4. Finally, key conclusions are summarized in Section 5.

2. METHODS

In this section, we provide an overview of the rfast atmospheric retrieval tool and the setup used to derive key properties from simulated reflected-light observations of Earth analogs. We also describe the observation scenarios, including the selection of spectral bandpasses and signal-to-noise ratio (S/N) considered for this study.

2.1. The rfast Atmospheric Retrieval Tool and Setup

We use rfast (Robinson & Salvador 2023; Salvador et al. 2024), a versatile atmospheric retrieval framework, to assess inferences of 17 unknown/free atmospheric and planetary properties (Table 1) out of synthetic observations of an Earth-analog orbiting a Sun-like star through various spectral bandpasses and S/N values (Table 2) proposed for HWO.

Future HWO observations will collect the light from the host star reflected by the planet directly imaged as a resolved and distinct light source. At a given star-planet-observer phase angle, α , it will measure the wavelength-dependent planet-to-star flux ratio, F_p/F_s , defined as:

$$\frac{F_{\rm p}}{F_{\rm s}} = A_{\rm g}\Phi(\alpha) \left(\frac{R_{\rm p}}{a}\right)^2 , \qquad (1)$$

where $A_{\rm g}$ is the geometric albedo, Φ is the phase function (which depends on the phase angle), $R_{\rm p}$ is the radius of the planet, and a is the orbital distance. The phase angle dependence, which defines the viewing angle geometry, is accounted for in rfast 3D mode (Robinson & Salvador 2023). The planet is treated as a homogeneous pixelated globe (such as a disco ball), where radiative transfer calculations are performed for each pixel under local plane-parallel approximation. Depending on the illumination geometry, each facet of the pixelated globe has different pairs of incidence and emergence angles. A Gauss-Chebyshev integration of the flux emitted by all plane-parallel facets gives the total emergent flux from the spatially-integrated illuminated disk/planet (e.g., Horak & Little 1965; Robinson & Salvador 2023; Salvador et al. 2024).

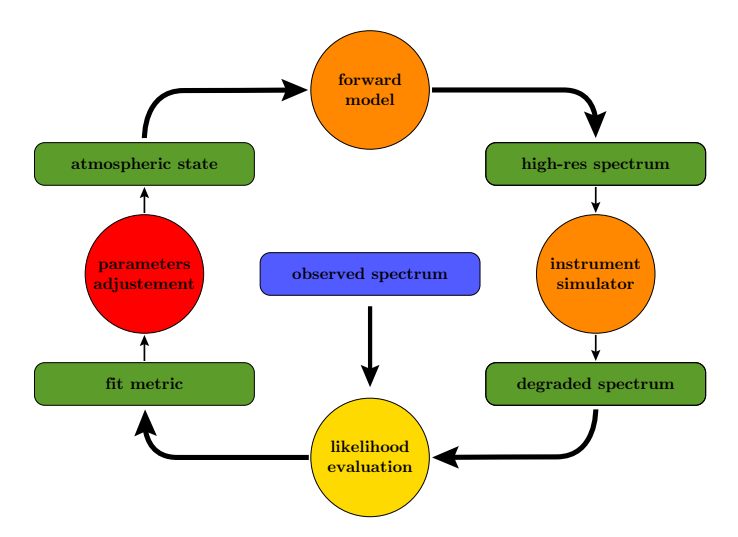


Figure 1. Schematic of the rfast retrieval framework. Boxes denote model inputs and outputs, while circles represent components of the framework. Here, the "observed" spectrum is a synthetic observation of an Earth analog, generated using Earth-based fiducial parameters (see Table 1).

Since the overriding goal of HWO is the characterization of Earth-like habitable exoplanets, we focus on observations of the best characterized habitable planet: Earth. The retrieval algorithm is depicted in Figure 1 and proceeds as follows. A radiative transfer "forward" model first generates a high-resolution reflected light spectrum of Earth based on its known (fiducial) properties (Table 1), i.e., with an atmospheric composition dominated by N₂ (78%) and O₂ (21%), with H₂O, CO₂, CH₄, and O₃ as additional trace species, and Ar as the background gas. Note that the forward model-generated reflected light spectrum has been validated against Earth observations (Robinson & Salvador 2023). An instrument model then degrades the resolution and adds noise to mimic a "faux observation" (Figure 2) for a given HWO design and for a given observation scenario (subsection 2.2). These synthetic observations are then compared to spectra generated in the same way, but using sets of free parameters (consistent with any specified prior ranges) sampled by a Bayesian tool (emcee; Foreman-Mackey et al. 2013). The likelihood of the sampled parameter values is assessed by how well the newly generated spectra reproduce the faux observations (Figure 2), via a standard chi-squared (χ^2) . When combined with the priors, this likelihood yields a posterior probability distribution for the parameters, which then informs how parameter space should be further explored. After a burn-in period, the posterior probability distribution of each free parameter indicates the parameter ranges that can explain the observations. To estimate remote sensing capabilities and accuracy of different observing scenarios, we repeat the same procedure considering observations for different spectral bandpasses and S/N (Table 2), and compare the retrieval results to one another.

Similar to Salvador et al. (2024), the 17 retrieved parameters (whose prior ranges and Earth-based fiducial values are listed in Table 1) define the surface conditions via the surface pressure ($p_{\rm surf}$) and albedo ($A_{\rm surf}$), the atmospheric thermal and chemical state via a characteristic atmospheric temperature (T; which is probed through the temperature dependence of the band shapes) and the atmospheric volume mixing ratios of N₂, O₂, H₂O, CO₂, CH₄, and O₃ (with Ar back-filling the rest of the atmosphere when the total volume mixing ratio is lower than one), as well as the cloud, orbital, and planetary bulk properties. The cloud properties are defined via the cloudiness fraction (f_c) and their top pressure (p_c), thickness (Δp_c), and optical depth (τ_c). The planetary bulk properties are the planet mass (M_p) and radius (R_p), and the orbital distance (a) and the planetary phase angle (a) are the orbital parameters.

The retrieval settings were as follows. The rfast Bayesian sampling tool emcee was set with 15 Markov Chain Monte Carlo chains (walkers) per parameter (for a total of 255 walkers). Starting from random values around the truth, we let emcee explore the parameter space within the range of values defined as flat priors (Table 1) for 100k steps (proven to be enough for the chains to fully converge for all retrieved parameters; Robinson & Salvador 2023; Salvador et al. 2024). We then draw the parameter posterior distributions from the last 5k steps, which gives a statistically representative sample without being computationally prohibitive. This is consistent with our previous studies (Feng et al. 2018; Robinson & Salvador 2023; Salvador et al. 2024) and ensures thorough exploration of the parameter space by the walkers, regardless of their initial position.

Our observation scenarios consist of combinations of various spectral bandpasses and qualities proposed for typical HWO/LUVOIR/HabEx setups (Table 2). We consider five different observation scenarios—"Red", "Blue & Red", "Visible", "vNIR", and "NIR" (see Table 2)—spanning both broad and narrow wavelength coverages to match instrument limitations and/or observation strategies that restrict or enhance access to spectral features indicative of habitability (e.g., The LUVOIR Team 2019; Young et al. 2024). Aligning with technical restrictions of coronagraphs, which operate over relatively limited bandpasses (e.g., $\lesssim 0.2$ μm -wide ranges in the visible), we include scenarios with either a single 20% coronagraph "Red" bandpass at red wavelengths ($\lambda = [0.87 - 1.05] \mu m$, spectral resolving power $res = \lambda/\delta\lambda = 140$; targeting the prominent 0.94 µm water vapor band) or two 20% coronagraph "Blue & Red" bandpasses—one at red wavelengths and one at blue wavelengths ($\lambda = [0.43 - 0.53] \mu m$, res = 140; highlighting Rayleigh scattering slopes, which help constrain planet size). A single red channel aligns with an early step in the LU-VOIR "search for life" strategy focused on detecting water vapor signatures (see, e.g., the 0.89 µm bandpass in Young et al. 2024), while the pair of Blue & Red channels corresponds to later steps emphasizing atmospheric characterization (see Figure 1.5 in The LUVOIR Team 2019). Note that, unless they are in parallel coronagraphs, these single channels must be observed sequentially (e.g., The LUVOIR Team 2019; Young et al. 2024). Beyond these restricted channels, we consider a "Visible" case with a broad bandpass (achievable with parallel coronagraph instruments or a starshade; Shaklan et al. 2023, 2024; Mennesson et al. 2024) covering the full visible/optical range ($\lambda = [0.45 - 1.0] \, \mu m$, res = 140) for spectroscopic characterization and minimizing false negative detections of life. An additional optimistic, very broad "vNIR" bandpass is included, spanning visible to near-infrared wavelengths ($\lambda = [0.45 - 1.8] \mu m$, with res = 70 in the NIR), consistent with in-depth follow up characterization of promising targets (The LUVOIR Team 2019). Such wide spectral coverage could be acquired either simultaneously via parallel coronagraph instruments for maximum efficiency (or sequentially for maximum sensitivity; The LUVOIR Team 2019), or via a single radial movement of the starshade to access near-infrared wavelengths in a HabEx-type architecture (Gaudi et al. 2020). Lastly, a "NIR"-restricted scenario (spanning $\lambda = [1.0 - 1.8] \, \mu \text{m}$, res = 70) is also considered to assess the value of these wavelengths.

For each observation scenario, we consider three different spectral qualities (i.e., S/N, that translates into exposure times for a specific instrument design), spanning the range from moderate (S/N = 10) to moderate-high quality (S/N = 20), with an intermediate case (S/N = 15). As in Salvador et al. (2024) and following Feng et al. (2018) initial validation, the noise is considered constant, nonrandomized (i.e., the error bars are simply centered on truth/noise-free values) and gray (i.e., wavelength-independent) to account for different data quality without being attached to specific observing parameters such as telescope diameter or target distance (as opposed to integration times; see Feng et al. 2018). The S/N value (10, 15, or 20) is set at the lower bound of each spectral bandpass (at $\lambda_0 = 0.87$, 0.43, and 1.0 μ m for the Red, Blue & Red, and NIR scenarios, respectively, and at $\lambda_0 = 0.45 \mu$ m for both the Visible and vNIR spectral bandpasses), and propagated across the entire spectral coverage while maintaining a constant noise/error bar size (shown on Figure 2 for each S/N value; see Appendix A for more details). The corresponding S/N value obtained as a function of wavelength for each spectral coverage is shown in Figure 8. On top of enabling easier reproducibility because of the wavelength independence, a constant gray noise aligns with the predicted performance of the HabEx and LUVOIR missions, assuming equal exposure times across their UV, optical, and NIR spectral bands (The LUVOIR Team 2019; Gaudi et al. 2020). Furthermore, Feng et al. (2018) demonstrated that for a statistical sampling of retrievals, a more realistic, randomized noise instance would yield similar inference results.

A novel approach adopted for the retrievals presented here assumes that spectral observations are acquired "early," meaning before orbit determination. In the absence of prior orbit constraints from precision radial velocity or host stellar astrometry, typical mission strategies involve multiple repeat photometric high-contrast imaging visits to planetary systems to constrain orbital parameters and identify worlds within the habitable zone of their host star. The "early" spectral characterization approach explored here represents a paradigm where spectroscopy is performed immediately after photometric detection, trading orbital information for the potential of earlier atmospheric species detection. One might call this the "spectrum first, ask questions sooner" approach.

With five variations of spectral coverages and three different S/N (Table 2), we considered a total of 15 different observation scenarios for which we ran retrieval analysis to assess their respective value in inferring the properties of Earth analogs and thus define the best observing strategy. The retrieval results are presented in the next section.

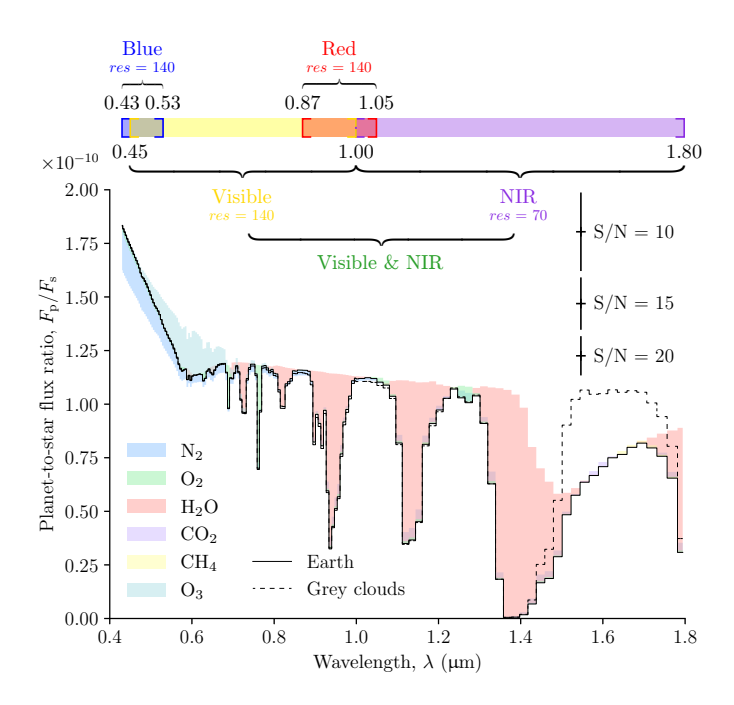


Figure 2. Model-generated (synthetic) reflected light spectrum of our fiducial case (plain line): an Earth-like planet at quadrature (i.e., at a planetary phase angle $\alpha=90^\circ$; see Table 1 for fiducial input values), and assuming grey cloud properties (dashed line), which notably do not capture the absorption feature of water ice clouds near 1.6 μm. The colored areas indicate the spectral imprints of the gas species by showing the difference between the baseline spectrum (plain line) and the flux measured if they were absent from the atmosphere and replaced with Ar, the background gas. The top of the figure indicates the spectral ranges considered, along with their resolving power $res=\lambda/\delta\lambda$ (Table 2): Blue ($\lambda=[0.43-0.53]$ μm, res=140) & Red ($\lambda=[0.87-1.05]$ μm, res=140) bandpasses, Visible ($\lambda=[0.45-1]$ μm, res=140) & near-infrared (NIR; $\lambda=[1-1.80]$ μm, res=70) bandpasses (together denoted vNIR), or Red, Visible, and NIR bandpasses observed individually. The error bars represent the nonrandomized, wavelength-independent noise levels corresponding to specific signal-to-noise ratios (S/N), set at the lower bound of each spectral coverage (see Appendix A and Figure 8): $\lambda_0=0.43$ μm for the Blue & Red bandpass, $\lambda_0=0.45$ μm for the Visible and Visible & NIR spectral ranges, $\lambda_0=0.87$ μm for the Red bandpass, and $\lambda_0=1.00$ μm for the NIR bandpass.

We first introduce our parameter inference classification—which defines the levels of constraints or detection strengths based on inference results and posterior distribution shapes—and, then, present the retrieval results for observations across the different spectral bandpasses (and their combinations). These results are shown in Figure 3, Figure 4, Figure 5, Figure 6, and Figure 7 for different parameter categories. Quantitative estimates are also provided in Table 6, Table 7, and Table 8 for S/N = 10, 15, and 20, respectively.

3.1. Parameter Inference Classification

Parameter inference accuracy is classified in 5 categories based on the shape of the posterior distribution and depending on the level of constraint obtained. Retrieved parameters can be any of the following (from highest to lowest accuracy):

- Constrained ("C"): the fiducial value is retrieved unequivocally. The posterior distribution typically exhibits a marked peak without tails extending toward extreme values, with the fiducial value included within the 68% confidence interval whose width is no larger than 1 log-unit (i.e., 1 order of magnitude) for log-scale prior ranges spanning at least 5 log-units, and no larger than 0.5 log-units otherwise. This is typically the case of the water vapor mixing ratio for observations in the visible or vNIR ranges from S/N = 15 (Figure 3). For linear-scale prior ranges, the 68% confidence interval width is contained within ±20% of the input value.
- Detected ("D"): the parameter is loosely constrained. The posterior distribution is peaked without tails toward extreme values but with a 68% confidence interval width larger than an order of magnitude ("detection" case of Feng et al. 2018). This is typically the case of the water vapor mixing ratio for observations in the visible or vNIR ranges at S/N = 10 (Figure 3).

Table 1. Retrieved Parameters, Corresponding Description, Earth-based Fiducial Input Value, and Prior Range

Parameter	Description	Input	Flat Prior
	Surface Condition	s	
$\log p_{\rm surf}$	Surface pressure (Pa)	$\log(10^{5})$	[0, 8]
T	Atmospheric temperature* (K)	255	[100, 1000]
$\log A_{\rm surf}$	Surface albedo	$\log(0.05)$	[-2, 0]
	Gas Abundances [†]		
$\log f_{N_2}$	Molecular nitrogen mixing ratio	$\log(0.78)$	[-10, 0]
$\log f_{O_2}$	Molecular oxygen mixing ratio	$\log(0.21)$	[-10, 0]
$\log f_{\rm H_2O}$	Water vapor mixing ratio	$\log(3\times10^{-3})$	[-10, 0]
$\log f_{\rm CO_2}$	Carbon dioxide mixing ratio	$\log(4\times10^{-4})$	[-10, 0]
$\log f_{\mathrm{CH_4}}$	Methane mixing ration	$\log(2\times10^{-6})$	[-10, 0]
$\log f_{\mathrm{O}_3}$	Ozone mixing ratio	$\log(7 \times 10^{-7})$	[-10, -2]
	Planetary Bulk Param	eters	
$\log R_{\rm p}$	Planet radius (R_{\oplus})	log(1)	[-1, 1]
$\log M_{ m p}$	Planet mass (M_{\oplus})	$\log(1)$	[-1, 2]
	Cloud Parameters	:	
$\log p_{\rm c}$	Cloud-top pressure (Pa)	$\log(6 \times 10^4)$	[0, 8]
$\log \Delta p_{\rm c}$	Cloud thickness (Pa)	$\log(10^4)$	[0, 8]
$\log \tau_{\rm c}$	Cloud optical depth	$\log(10)$	[-3, 3]
$\log f_{\rm c}$	Cloudiness fraction	$\log(0.5)$	[-3, 0]
	Orbital Parameter	s	
a	Planetary orbital distance (AU)	1	[0.1, 10]
α	Planetary phase angle (°)	90	[0, 180]

^{*}Isothermal atmosphere temperature.

Table 2. Retrieval Grid: Wavelength Coverages and Spectral Qualities Explored in This Study

Wavelength Coverage						
Case description	λ range (μ m)	Resolving power $res = \lambda/\delta\lambda$				
Blue & Red	[0.43 - 0.53] & [0.87 - 1.05]	140 & 140				
Red	[0.87 - 1.05]	140				
Visible	[0.45 - 1.00]	140				
NIR	[1.00 - 1.80]	70				
${\rm vNIR}$ (Visible & NIR)	[0.45 - 1.00] & [1.00 - 1.80]	140 & 70				
	$Spectral\ Quality^*$					
Moderate		$S/N_{\lambda_0} = 10$				
Intermediate	$S/N_{\lambda_0} = 15$					
Moderate-high		$S/N_{\lambda_0} = 20$				

^{*}The S/N value is set at the lower bound of each spectral coverage

- Weakly detected ("WD"): a restricted range of values are favored, but extreme values are not excluded. The posterior distribution has a marked peak but a 68% confidence interval width larger than an order of magnitude and also a substantial tail toward extreme values ("weak detection" case of Feng et al. 2018 and equivalent to the "sensitivity limit" case of Konrad et al. 2022). An illustrative example is the posterior distribution of the molecular oxygen mixing ratio for observations in the visible or vNIR ranges at S/N = 10 (Figure 3).
- Limited by upper or lower bounds ("L"): values above/below an upper/lower threshold are excluded, but the parameter can equally take any other value. The posterior distribution has no marked peak and is flat across a limited portion of the prior range ("upper limit" type of Konrad et al. 2022). The posterior distributions of the methane mixing ratio exhibit a clear upper limit for observations in the vNIR at any S/N value (Figure 3).
- Not constrained ("NC"): all parameter values are equally likely across the prior range, i.e., the parameter can take any value over the specified range. The posterior distribution is flat across the entire (or nearly) prior range

 $^{^\}dagger \mbox{The remaining atmosphere is back-filled with argon.}$

⁽e.g., $\lambda_0 = 0.45 \,\mu\text{m}$ for the Visible and vNIR ranges; see Appendix A).

See Figure 8 for the corresponding S/N as a function of wavelength.

("nondetection" case and "unconstrained" type of Feng et al. 2018 and Konrad et al. 2022, respectively). The molecular nitrogen mixing ratio is typically not constrained in all retrieval scenarios presented here (Figure 3).

3.2. Gas Abundances

Figure 3 shows the retrieval results of the atmospheric composition. Gas abundance retrieval accuracy generally correlates with the presence and strength of absorption and spectral features within the observed spectral bandpass (Figure 2). Prominent absorption features exist in each spectral range (except in the Blue; Figure 2) and enable retrievals to provide at least lower limits on the atmospheric water vapor mixing ratio, regardless of the S/N (Figure 3). For spectra of moderate quality (S/N = 10), a water vapor mixing ratio of at least $f_{\rm H_2O} \gtrsim 10^{-6}$ is necessary to explain the observed spectrum and its water vapor absorption features in the Red, Blue & Red, and NIR bandpasses. However, for these spectral coverages, further increases in S/N do not significantly improve inferences of water vapor concentration due to degeneracies with the abundance of other absorbers and cloud properties—especially cloud altitude (e.g., high-altitude clouds could make up for lower water vapor concentrations)—in the NIR (Figure 10). In contrast, firm detections of water vapor concentration can be achieved even at S/N = 10 for observations covering broad spectral ranges in the visible (i.e., visible-only and vNIR), which benefit from constraints on other parameters—such as ozone and oxygen concentrations—that help break degeneracies (Figure 9). Furthermore, the water vapor mixing ratio can be constrained at an S/N of 15 for these spectral coverages.

Similar reasoning applies to the retrievals of ozone and molecular oxygen abundances, whose primary spectral features are found in the Visible bandpass, with minor absorption features for oxygen in the NIR. As a result, the ozone mixing ratio can be constrained from observations spanning the visible (i.e., Visible and vNIR) at any S/N. An upper limit for f_{O_3} is obtained from observations in the combined Blue & Red bandpass, but it cannot be constrained from the Red or NIR bandpasses, regardless of the S/N. Oxygen has narrower spectral imprints than ozone, and due to the lack of significant spectral features in the red/blue bandpasses, it can only be weakly detected from observations in the Visible (owing mainly to the O_2 A-band centered at 0.762 μ m) and vNIR bandpasses. A minimum S/N = 20 in the Visible and S/N = 15 in the vNIR is required to fully constrain f_{O_2} . It cannot be constrained from observations in the Red, NIR, or Blue & Red bandpasses, regardless of the S/N.

Due to minor absorption features predominantly located in the NIR, retrievals can only place upper limits on the carbon dioxide abundance from observations in the NIR and vNIR bandpasses, with only marginal improvements in the latter. In the remaining spectral bandpasses analyzed, where CO_2 is relatively transparent, f_{CO_2} cannot be constrained. Across all spectral coverages, increasing the S/N does not significantly improve the retrievals of f_{CO_2} . Regardless of the selected spectral bandpass, only upper limits can be placed on the methane abundance, with minor improvements from observations in the vNIR. Increasing the S/N does not significantly affect the retrievals of f_{CH_4} . This is in agreement with previous studies showing that modern-Earth methane concentration is not detectable (e.g., Kawashima & Rugheimer 2019; Latouf et al. 2024).

Because of the absence of associated absorption features, the atmospheric abundance of molecular nitrogen can virtually take any value from $f_{\rm N_2} = 10^{-10}$ to $f_{\rm N_2} = 1$ (Figure 3) and still produce a reflected-light spectrum that matches the observations. The lack of any apparent correlation with other parameters (e.g., Figure 9, Figure 10) indicates that the atmosphere can be filled interchangeably with argon (the assumed background gas) or with molecular nitrogen. As a result, the abundance of molecular nitrogen cannot be constrained.

Overall, regarding the atmospheric composition, only $f_{\rm H_2O}$, $f_{\rm O_3}$, and $f_{\rm O_2}$ can be effectively constrained, with strong sensitivity to the spectral region observed and only a weak influence of the S/N. This agrees with the results of Susemiehl et al. (2023); Latouf et al. (2023a,b), who used alternative restricted bandpasses. However, their more limited number of retrieved parameters may underestimate degeneracies that arise in retrievals with larger parameter spaces, potentially leading to artificially narrow posterior constraints. For the abundance of carbon dioxide and methane, only upper limits can be determined, while the abundance of N₂ cannot be constrained in any of the observation scenarios. We note that despite general agreement across recent retrieval studies (Feng et al. 2018; Damiano & Hu 2022; Susemiehl et al. 2023; Latouf et al. 2023a,b), there are noticeable differences in the reported detection significances and the S/N thresholds required. For instance, while our study finds only weak detections of O₂ at S/N = 10–15 in the visible range, Feng et al. (2018) report O₂ detection in the same configuration (though defining S/N at a slightly different reference wavelength: 0.55 μ m compared to 0.45 μ m in the present study), and Latouf et al. (2023b) report strong O₂ detections from S/N = 8 for 20% width bandpasses centered between 0.68 and 0.84 μ m. These discrepancies likely arise from a combination of factors, including differences in bandpass choices, S/N reference wavelengths and

definitions, the number of free parameters, assumptions about background gas composition, MCMC convergence, and how detection significance is defined. A systematic intercomparison of retrieval assumptions and frameworks would be valuable to clarify these differences and establish more standardized benchmarks.

3.3. Surface and Atmospheric Conditions

Both the surface pressure and atmospheric temperature are at least weakly detected for any combination of spectral coverage and S/N (Figure 4). The surface pressure is best retrieved for observations including the visible range (i.e., Visible and vNIR): it is detected for S/N values of 10 and 15, and becomes constrained at S/N = 20. For the characteristic atmospheric temperature, the best constraints come from observations including the NIR (i.e., vNIR and NIR), or part of it (i.e., Red). Both for observations restricted to the NIR or combined with the visible range, the temperature is detected at S/N = 10 and constrained from S/N = 15. It can be also detected and even constrained from observations in the Red bandpass at S/N = 15 and S/N = 20, respectively. Conversely, the surface albedo is at most weakly detected, and requires observations covering as much visible range as possible to obtain upper limits. Increasing the S/N does not improve albedo characterization. The weak detections obtained for observations in the Visible bandpass come from the emergence of a peak in the posterior distribution. Yet, this peak systematically overestimates the surface albedo, favoring planets brighter than they actually are.

3.4. Cloud Parameters

Earth's realistic water ice and liquid clouds optical properties are parameterized with wavelength-dependent scattering properties and a Henyey-Greenstein phase function (Robinson & Salvador 2023). A cloud asymmetry parameter and single-scattering albedo are used to reproduce their spectral imprint in Earth's spectrum. Notably, Earth's water ice clouds absorb in the NIR, near 1.6 μ m (e.g., Robinson et al. 2011), which explains why removing all atmospheric species still leaves a pit relative to the continuum in that region (see Figure 2 and the differences between the fiducial reflected-light spectrum and the one assuming grey cloud properties). Because of this cloud optical properties-related spectral feature in the NIR, cloud optical depth, cloud-top pressure, and cloudiness fraction are always at least weakly detected for observations spanning the NIR, regardless of the S/N (Figure 5). While these parameters are not accurately retrieved for observations conducted solely in the visible range, combining the Visible with the NIR gives the most accurate estimations, as seen by the shrinking tails of the posterior distributions and their narrowing toward the fiducial values, which are increasingly improved with increasing S/N. Notably, observations in the vNIR allow the cloudiness fraction to be constrained from S/N = 20 (weakly detected otherwise), the cloud-top pressure from S/N = 15 (already detected at S/N = 10), and the cloud optical depth from S/N = 10. In contrast, retrievals of cloud thickness are not strongly sensitive to the observed spectral region or S/N—although increasing the S/N to 20 slightly refines the upper boundary—and only very thick clouds can be excluded.

3.5. Planetary Bulk Parameters and Orbital Parameters

Retrievals of the planetary bulk parameters are not sensitive to the spectral coverage or S/N (Figure 6). Indeed, regardless of the observed spectral region or S/N, the planetary radius can only be weakly detected and is consistently overestimated. Observations in the Visible bandpass provide the best, though still unsatisfactory, lower limit. Note that Salvador et al. (2024) recently demonstrated that prior knowledge of the orbital parameters would allow tight constraints on the planetary radius. In contrast, the planetary mass cannot be constrained in any of the proposed scenarios.

The orbital parameters are also poorly constrained from reflected-light observations (Figure 7). Due to their strong degeneracy with the planetary radius (as demonstrated by Nayak et al. 2017; Salvador et al. 2024), and in the absence of any constraint on the latter, only a rough upper limit can be placed on the planetary phase angle. The orbital distance is at most weakly detected, with its posterior distribution peaking towards Earth-like values.

4. DISCUSSION

Based on the retrieval results described above, Table 3 shows the inference level obtained for each retrieved parameter as a function of the spectral coverage and S/N, and Table 4 summarizes the minimum observation requirements (in terms of spectral coverage and S/N) that HWO needs to meet to achieve the best possible level of constraint for each retrieved parameter. Reciprocally, the relative assets of each spectral coverage and S/N combination are shown in Table 5 and discussed in subsection 4.2. In subsection 4.3, we assess the value of early spectral characterization

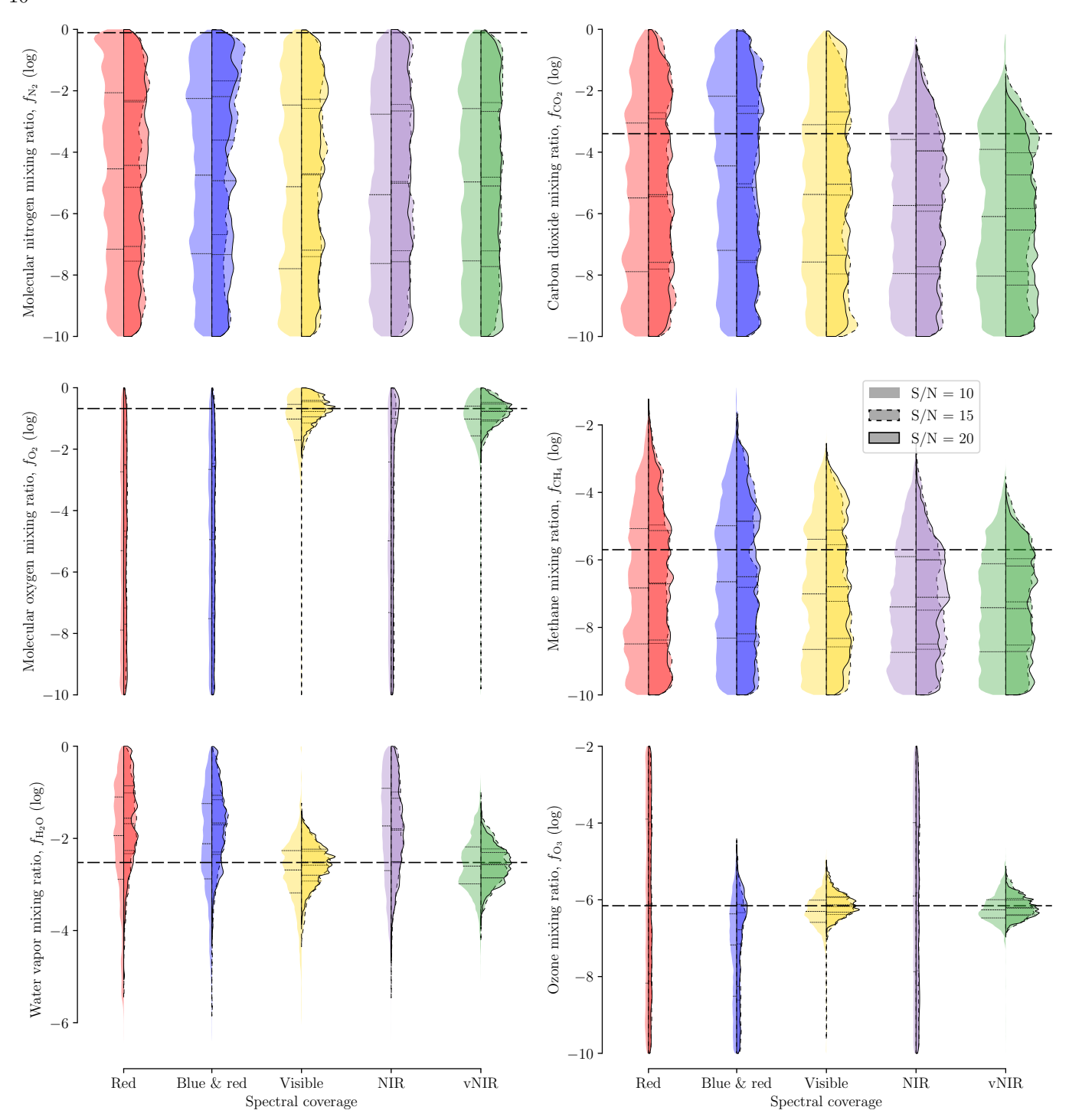


Figure 3. Posterior distributions of gas abundances obtained from observations in different color-coded spectral coverages at signal-to-noise ratios (S/N) of 10 (left side of the split-violins, without contour lines), 15 (right side, with dashed contours), and 20 (right side, with solid contours). From top to bottom: (left column) molecular nitrogen, molecular oxygen, water vapor, (right column) carbon dioxide, methane, and ozone. The horizontal dashed lines spanning each violin row indicate Earth-like input values, while the dashed lines within the violins show the 25th, 50th, and 75th percentiles of the data (the first quartile, median, and third quartile, respectively). The density has been normalized across all kernel density plots so that each has the same area.

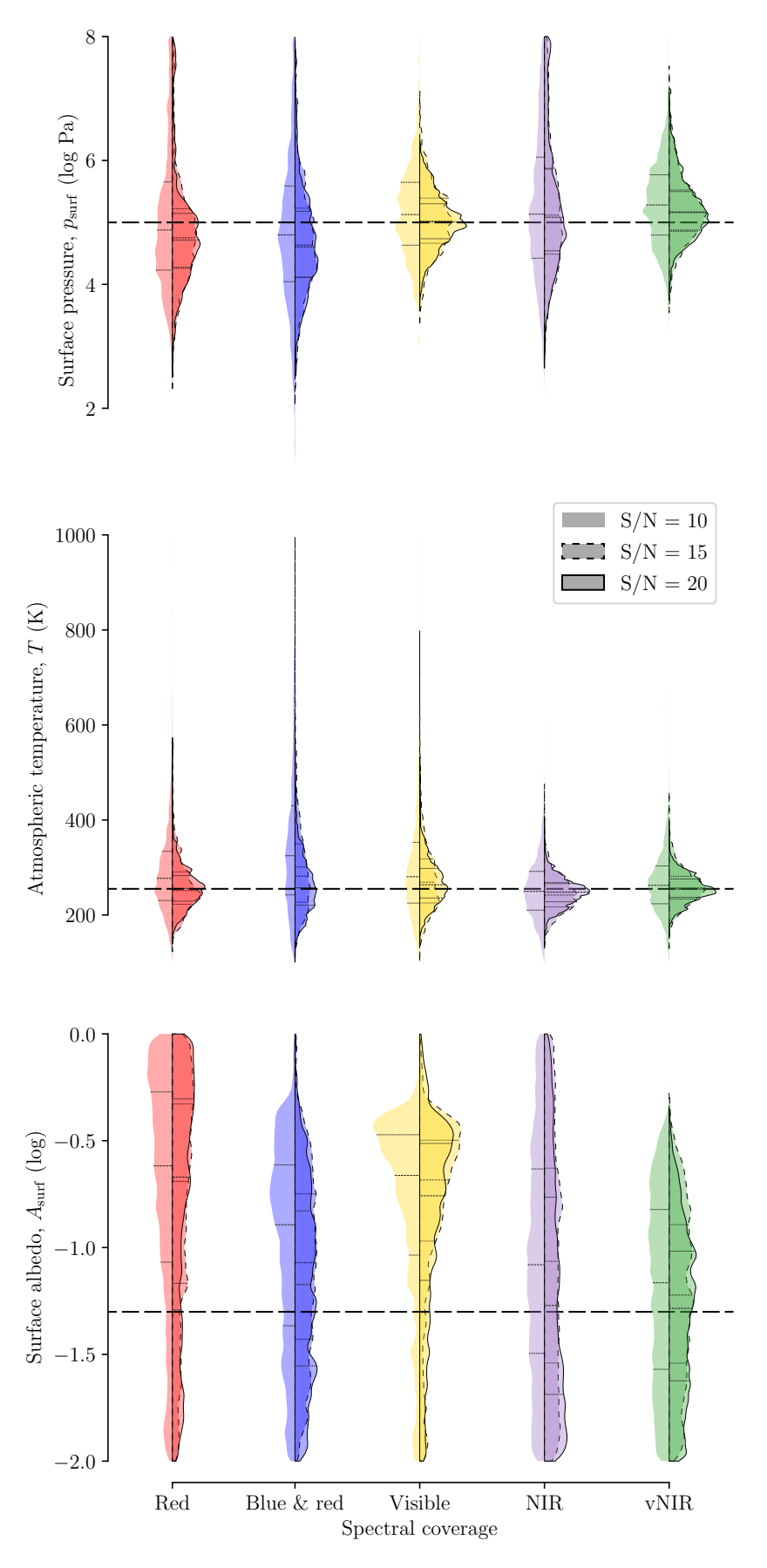


Figure 4. Posterior distributions of surface and atmospheric condition parameters obtained from observations in different color-coded spectral coverages at signal-to-noise ratios (S/N) of 10 (left side of the split-violins, without contour lines), 15 (right side, with dashed contours), and 20 (right side, with solid contours). From top to bottom: surface pressure, atmospheric temperature, and surface albedo. The horizontal dashed lines spanning each violin row indicate Earth-like input values, while the dashed lines within the violins show the 25^{th} , 50^{th} , and 75^{th} percentiles of the data (the first quartile, median, and third quartile, respectively). The density has been normalized across all kernel density plots so that each has the same area.

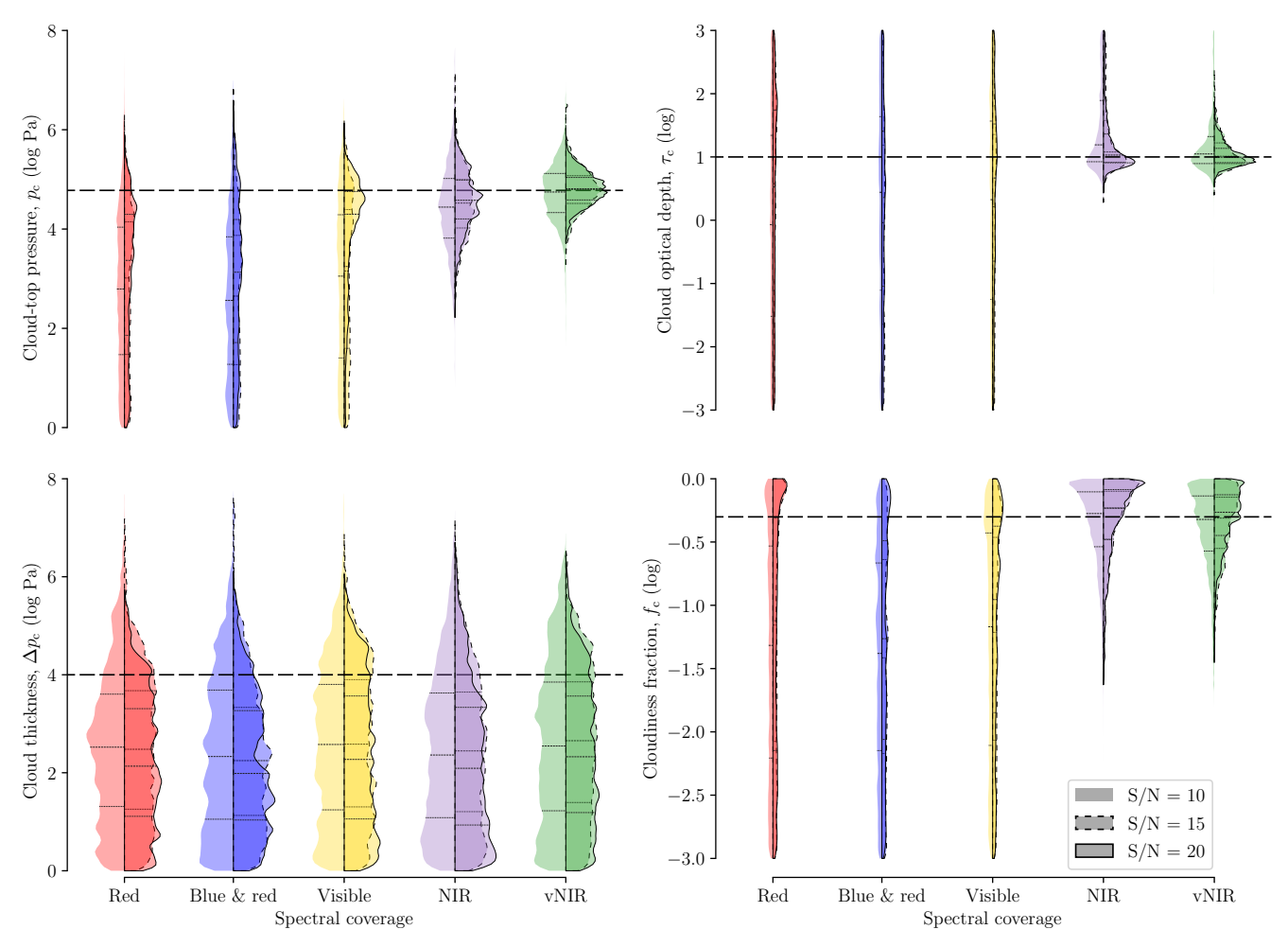


Figure 5. Posterior distributions of cloud properties obtained from observations in different color-coded spectral coverages at signal-to-noise ratios (S/N) of 10 (left side of the split-violins, without contour lines), 15 (right side, with dashed contours), and 20 (right side, with solid contours). From top to bottom: (left column) cloud-top pressure, thickness, (right column) optical depth, and cloudiness fraction. The horizontal dashed lines spanning each violin row indicate Earth-like input values, while the dashed lines within the violins show the 25th, 50th, and 75th percentiles of the data (the first quartile, median, and third quartile, respectively). The density has been normalized across all kernel density plots so that each has the same area.

prior to orbit determination, and in subsection 4.4, we discuss the implications of our findings for future observatory architectures.

4.1. Observation Requirements for the Retrieved Parameters

Summarizing our results, Table 3 and Table 4 show that from the atmospheric composition, only H_2O , O_2 , and O_3 can be constrained and require observations spanning at least the Visible bandpass. In the absence of retrieval degeneracies when a large set of parameters are inferred or if more parameters are constrained, this could possibly be achieved with alternative restricted bandpasses than the ones presented here (Susemiehl et al. 2023; Latouf et al. 2023a,b). Complementary observations in the mid-infrared would provide additional and missing constraints on the CO_2 and CH_4 abundances (e.g., Konrad et al. 2022; Alei et al. 2024), thus capturing a comprehensive picture of the atmospheric composition.

Except for the cloud thickness that is only limited and underestimated, cloud properties can be at least weakly detected from the NIR, and up to constrained when it is combined with the Visible. Regarding the surface conditions, the surface pressure is always at least weakly detected. It is detected for observations spanning the visible band (i.e., Visible and vNIR) at moderate (S/N = 10) and intermediate spectral quality (S/N = 15) and is constrained from S/N = 20. The characteristic atmospheric temperature is at least weakly detected in the Visible, Blue & Red, and Red bandpass cases, and becomes detected and constrained with increasing S/N in the latter. When the NIR is included,

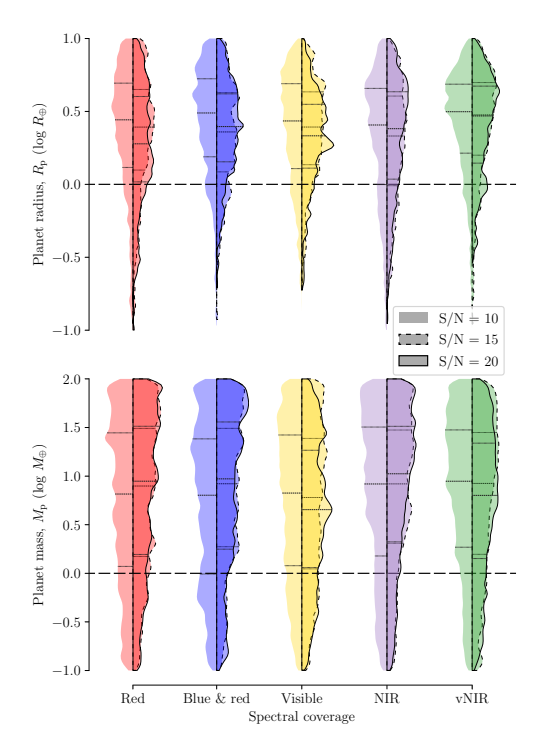


Figure 6. Posterior distributions of the planet radius (top) and mass (bottom) obtained from observations in different color-coded spectral coverages at signal-to-noise ratios (S/N) of 10 (left side of the split-violins, without contour lines), 15 (right side, with dashed contours), and 20 (right side, with solid contours). The horizontal dashed lines spanning each violin row indicate Earth-like input values, while the dashed lines within the violins show the 25th, 50th, and 75th percentiles of the data (the first quartile, median, and third quartile, respectively). The density has been normalized across all kernel density plots so that each has the same area.

the temperature value is detected from moderate quality (S/N = 10) observations, and accurately constrained from S/N = 15. Surface albedo inference can only be achieved with observations spanning a broad optical range, but is at most weakly detected and overestimated from observations in the Visible only. The most realistic estimates come from observations in the vNIR, but they only provide an upper limit.

The planetary radius is weakly detected at best and is typically overestimated, mistakenly favoring Neptune-sized planets. Prior information on the orbit (Salvador et al. 2024), mid-infrared observations (Konrad et al. 2022), or upcoming transit surveys (such as PLATO; Rauer et al. 2014, 2016, 2024) could help address this limitation, enabling more precise radius measurements – although both direct imaging and transit observations would only be feasible for a restricted subset of targets (Stark et al. 2020). Extreme Precision Radial Velocity could constrain the planetary mass (e.g., Plavchan et al. 2015), which is never constrained by the reflected-light observation scenarios proposed here. Similarly, the orbital parameters will require multiple reflected light observations over the course of the orbit, transit photometry, radial velocity measurements or astrometry to be more than weakly detected (in the Blue & Red, Visible, and NIR cases, and at high S/N in the Red bandpass) for the orbital distance, and better than limited (in all cases except for low S/N observations in the Red) for the planetary phase angle.

4.2. Detection Capabilities of the Different Observation Scenarios

Table 5 provides the detection capabilities of each spectral coverage and S/N combination for the proposed observation scenarios.

Observations through coronagraph-restricted spectral bandpasses (i.e., Red and Blue & Red) provide little information about the planet atmospheric and bulk properties. The atmospheric composition cannot be retrieved as atmospheric abundance constraints are at most limited (only for H_2O and CH_4). This is also true for NIR-only observations. It should be noted that despite being centered on one of its absorption bands, observations in the Red bandpass at most limit the possible range of water vapor abundance. However, assuming alternative bandpass centers with restricted bandwidth could yield better results and allow the detection of H_2O , O_2 , and O_3 (Susemiehl et al. 2023; Latouf et al. 2023a,b). Apart from the detection of the characteristic atmospheric temperature at S/N = 15

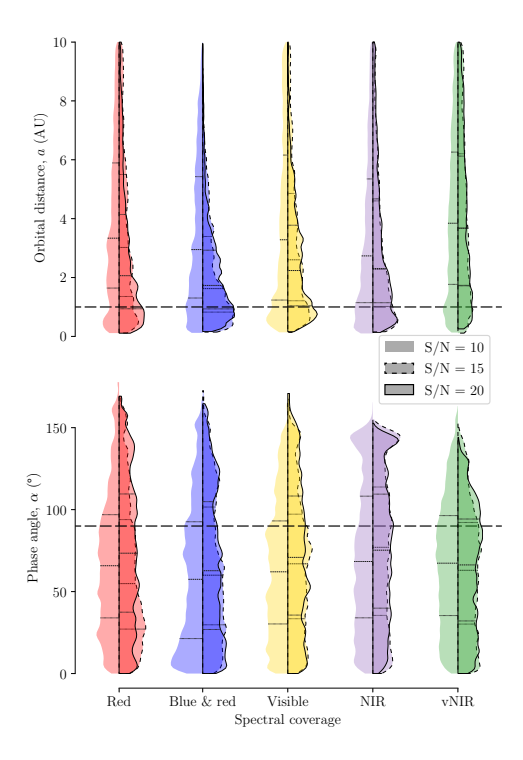


Figure 7. Posterior distributions of the orbital distance (top) and planetary phase angle (bottom) obtained from observations in different color-coded spectral coverages at signal-to-noise ratios (S/N) of 10 (left side of the split-violins, without contour lines), 15 (right side, with dashed contours), and 20 (right side, with solid contours). The horizontal dashed lines spanning each violin row indicate Earth-like input values, while the dashed lines within the violins show the 25th, 50th, and 75th percentiles of the data (the first quartile, median, and third quartile, respectively). The density has been normalized across all kernel density plots so that each has the same area.

and its constraint at S/N = 20 with the Red bandpass, coronagraph-restricted observations at best allow only weak detections of the surface pressure, temperature, planet radius, and orbital distance (only at S/N = 20 in the Red bandpass), and this, regardless of S/N. Adding the Blue bandpass to the Red one improves ozone abundance inference by placing an upper limit and significantly restricting the range of possible values. With increasing S/N, the posterior distribution peaks towards the fiducial value, indicating that it could possibly be retrieved at higher S/N. When adding the Blue bandpass, the inference of the surface albedo is also improved with a 68% confidence interval shifting towards the fiducial value and an upper limit excluding overly bright planets favored with the Red bandpass. Despite these improvements, the parameters are at most weakly detected in the Blue & Red scenario.

The Visible range is critical for detecting key atmospheric species such as H_2O , O_2 , and O_3 , and constraining their abundance when increasing the S/N. None of the other spectral bandpasses alone achieve weak detection for any of the atmospheric component, even at S/N = 20. This range also needs to be included to detect (S/N = 10 and 15) and constrain (at S/N = 20) the surface pressure, which can only be weakly detected otherwise.

NIR-only observations provide the strongest constraints on the characteristic atmospheric temperature even from low S/N, and are required to infer cloud properties. Indeed, the cloud fraction, optical depth, and cloud-top pressure can only be retrieved from observations including the NIR.

Combining the Visible and NIR (vNIR) thus provides the most comprehensive atmospheric characterization, by achieving constraints on key atmospheric species (i.e., H₂O, O₂, and O₃; obtained from the Visible), surface pressure and temperature, as well as inferring cloud properties (i.e., top pressure, optical depth, and fraction; from the NIR). In addition, while adding the NIR to the Visible seems to degrade the surface albedo inference from our detection strength classification, the switch from an overestimated weak detection in the Visible to an upper limit in the vNIR actually favors values closer to the fiducial one, which is then included within the 68% confidence interval. However, it should be noted that the orbital distance inference becomes depreciated in the vNIR compared to Visible- or NIR-only observations (from weakly detected with a slight peak in the distribution to not constrained).

Table 3. Observation Requirements for Each Retrieved Parameter

Parameter	S/N	Red	Blue & Red	Visible	NIR	vNIR
1 arameter	10	NC	NC	NC	NC	NC
f_{N_2}	15	NC	NC	NC	NC	NC
	20	NC	NC	NC	NC	NC
	10	NC	NC	WD	NC	WD
$f_{\mathcal{O}_2}$	15	NC	NC	WD	NC	C
JO_2	20	NC	NC	C	NC	C
-	10	L	L	D	L	D
$f_{ m H_2O}$	15	L	L	C	L	C
J112O	20	L	L	C	L	C
	10	NC	NC	NC	L	L
$f_{\rm CO_2}$	15	NC	NC	NC	L	L
7002	20	NC	NC	NC	L	L
	10	L	L	L	L	L
$f_{\mathrm{CH_4}}$	15	L	L	L	L	L
J 0114	20	L	L	L	L	L
	10	NC	L	C	NC	C
$f_{{ m O}_3}$	15	NC	L	C	NC	C
J O 3	20	NC	L	C	NC	C
	10	WD	WD	D	WD	D
$p_{ m surf}$	15	WD	WD	D	WD	D
rsuii	20	WD	WD	C	WD	C
	10	WD	WD	WD	D	D
T	15	D	WD	WD	C	C
	20	C	WD	WD	C	C
	10	NC	L	WD	NC	L
$A_{ m surf}$	15	NC	L	WD	NC	L
	20	NC	L	WD	NC	L
	10	WD	WD	WD	WD	WD
$R_{\rm p}$	15	WD	WD	WD	WD	WD
	20	WD	WD	WD	WD	WD
	10	NC	NC	NC	NC	NC
$M_{ m p}$	15	NC	NC	NC	NC	NC
	20	NC	NC	NC	NC	NC
	10	L	L	L	WD	D
$p_{ m c}$	15	L	L	L	WD	C
	20	L	L	WD	D	C
	10	L	L	L	L	L
$\Delta p_{ m c}$	15	L	L	L	L	L
	20	L	L	L	L	L
	10	NC	NC	NC	WD	C
$ au_{ m c}$	15	NC	NC	NC	WD	С
	20	NC	NC	NC	С	С
	10	NC	NC	NC	WD	WD
$f_{ m c}$	15	NC	NC	NC	WD	WD
	20	NC	NC	NC	WD	С
	10	NC	WD	WD	WD	NC
a	15	NC	WD	WD	WD	NC
	20	WD	WD	WD	WD	NC
	10	NC	L	L	L	L
α	15	L	L	L	L	L
	20	L	L	L	L	L

Table 4. Minimum Observation Requirements, i.e., Narrowest Spectral Coverage and Lowest S/N, to Achieve the Best Possible Inference of Atmospheric and Bulk Properties of Earth-Analogs

Parameter	Spectral Coverage	S/N	Best Inference	
	Surface Conditions			
Surface pressure, p_{surf}	Visible	20	Constraint	
Atmospheric temperature, T	NIR/Red	15/20	Constraint	
Surface albedo, A_{surf}	Visible	10	Weak Detection*	
	Gas Abundances			
Molecular nitrogen mixing ratio, f_{N_2}	NA	NA	No Constraint	
Molecular oxygen mixing ratio, $f_{\rm O_2}$	vNIR/Visible	15/20	Constraint	
Water vapor mixing ratio, $f_{\rm H_2O}$	Visible	15	Constraint	
Carbon dioxide mixing ratio, $f_{\rm CO_2}$	NIR	10	Limit	
Methane mixing ration, $f_{\rm CH_4}$	NA	NA	Limit	
Ozone mixing ratio, $f_{\rm O_3}$	Visible 10		Constraint	
	Planetary Bulk Parameters			
Planet radius, $R_{\rm p}$	NA	NA		
Planet mass, $M_{\rm p}$	NA	NA	No Constraint	
	Cloud Parameters			
Cloud-top pressure, $p_{\rm c}$	m vNIR	15	Constraint	
Cloud thickness, $\Delta p_{\rm c}$	NA	NA	Limit	
Cloud optical depth, $\tau_{\rm c}$	vNIR/NIR	10/20	Constraint	
Cloudiness fraction, f_c	vNIR	20	Constraint	
	Orbital Parameters			
Planetary orbital distance, a	Red/Blue & Red/Visible/NIR	20/10/10/ 10		
Planetary phase angle, α	Red/Blue & Red/Visible/NIR	15/10/10/ 10	Limit	

Notes.

See subsection 3.1 for the inference classification.

Not Applicable (NA) for parameters whose inference does not change with the spectral coverage or S/N.

*Overly bright planets are favored from observations in the Visible. While only placing an upper limit, vNIR observations provide better surface albedo inferences (see Figure 4 and subsection 4.2).

None of the spectral bandpass and S/N combinations considered here allow retrieval of the planetary bulk properties. While the planetary mass is never constrained, the weak detection of the planet's radius mistakenly favors large planets over Earth-sized ones (as emphasized in Salvador et al. 2024). This highlights the importance of prior determination of the orbit (which cannot be achieved in any of the observation scenarios presented here) to break its degeneracy with the radius, thereby enabling accurate inference of the radius and correct identification of Earth-sized planets (Salvador et al. 2024).

4.3. Assessment of the Value of Early Spectral Observations in Unconstrained Orbits

Our results suggest that the identification and comprehensive characterization of a habitable environment—including the detection of key atmospheric species, potential biomarkers, and constraints on surface conditions (P_{surf} and T)—can be achieved even without prior knowledge of the planet's orbit, provided early spectral observations span the Visible range. Specifically, observations in this range enable inference of H_2O , O_2 , and O_3 abundances, as well as surface pressure.

Spanning the NIR is critical to infer cloud properties and atmospheric temperature. Combined with the Visible range, this spectral breadth maximizes the observation returns even at moderate S/N of 10. Such broad spectral

coverage allows inference of important parameters—including key atmospheric species $(H_2O, O_2, and O_3)$, surface pressure, atmospheric temperature, cloud fraction, optical depth, and cloud-top pressure—demonstrating that much of the planet's thermo-chemical environment can be characterized prior to orbit determination.

However, even at moderate-to-high quality (S/N = 20), early spectral observations confined to coronagraph-restricted bandpasses (Red and Blue & Red) can only place limits on the abundance of certain atmospheric species ($\rm H_2O$, $\rm O_3$, and $\rm CH_4$) and weakly detect surface conditions. Such narrow bandpass observations are insufficient to provide firm constraints on the planet's habitable potential. Note that alternative restricted bandpasses have been shown to be promising (Susemiehl et al. 2023; Latouf et al. 2023a,b), but their detection capabilities should further be tested with a larger number of unconstrained parameters.

Given these considerations, a viable observation strategy is to perform early spectral observations, immediately following the initial photometric survey of a system, on any candidates with contrast ratios consistent with rocky planets. An additional consideration for prioritizing spectral observations in these systems could be a planet's projected separation from its host star, which is likely to be similar to its orbital semi-major axis (Guimond & Cowan 2019). It may be the case, though, that two photometric visits to the system spaced closely in time are required to ensure sources are co-moving. Information gained from these spectra can then prioritize targets for more detailed orbital and spectral follow-up, reducing the need for multiple photometric visits to lower-priority worlds. In the future, direct imaging yield calculation tools (e.g., Stark et al. 2019; Morgan et al. 2022; Stark et al. 2024; Morgan et al. 2024) could assess if an "early spectral characterization" model achieves more opportunities for studying potentially Earth-like worlds.

Critically, in this "spectrum first" approach, the choice of spectral bandpass is more important than increasing S/N (in agreement with previous studies considering different levels of prior constraints; Damiano & Hu 2022; Damiano et al. 2023; Susemiehl et al. 2023; Latouf et al. 2023a,b). The ability to infer a planet's thermo-chemical environment and habitability potential depends more strongly on broad spectral coverage than on higher S/N observations confined to narrower bandpasses.

Spectral Coverage	Detection Strength	S/N = 10	S/N = 15	S/N = 20
	No Constraint	$f_{\rm N_2}, f_{\rm O_2}, f_{\rm CO_2}, f_{\rm O_3}, A_{\rm surf}, M_{\rm p}, \tau_{\rm c}, f_{\rm c}, a, \alpha$	$f_{\rm N_2}, f_{\rm O_2}, f_{\rm CO_2}, f_{\rm O_3}, A_{\rm surf}, M_{\rm p}, \tau_{\rm c}, f_{\rm c}, a$	$f_{\rm N_2}, f_{\rm O_2}, f_{\rm CO_2}, f_{\rm O_3}, A_{\rm surf}, M_{\rm p}, \tau_{\rm c}, f_{\rm c}$
Red	Limited	$f_{\rm H_2O}, f_{\rm CH_4}, p_{\rm c}, \Delta p_{\rm c}$	$f_{\rm H_2O}$, $f_{\rm CH_4}$, $p_{\rm c}$, $\Delta p_{\rm c}$, α	$f_{\rm H_2O}$, $f_{\rm CH_4}$, $p_{\rm c}$, $\Delta p_{\rm c}$, α
$\lambda = [0.87 - 1.05] \mu \text{m}$	Weak Detection	$p_{\rm surf}, T, R_{\rm p}$	$p_{\mathrm{surf}}, R_{\mathrm{p}}$	$p_{\text{surf}}, R_{\text{p}}, a$
[0.0100]	Detection		T	
	Constraint			T
Blue & Red	No Constraint	$f_{\rm N_2}, f_{\rm O_2}, f_{{\rm CO}_2}, M_{\rm p}, au_{\rm c}, f_{\rm c}$	$f_{\rm N_2}, f_{\rm O_2}, f_{\rm CO_2}, M_{\rm p}, \tau_{\rm c}, f_{\rm c}$	$f_{\rm N_2}, f_{\rm O_2}, f_{{\rm CO}_2}, M_{\rm p}, \tau_{\rm c}, f_{\rm c}$
$\lambda = [0.43 - 0.53] \&$	Limited	$f_{\rm H_2O}$, $f_{\rm CH_4}$, $f_{\rm O_3}$, $A_{\rm surf}$, $p_{\rm c}$, $\Delta p_{\rm c}$, α	$f_{\rm H_2O}$, $f_{\rm CH_4}$, $f_{\rm O_3}$, $A_{\rm surf}$, $p_{\rm c}$, $\Delta p_{\rm c}$, α	$f_{\rm H_2O}$, $f_{\rm CH_4}$, $f_{\rm O_3}$, $A_{\rm surf}$, $p_{\rm c}$, $\Delta p_{\rm c}$, α
[0.87 – 1.05] μm	Weak Detection	$p_{\rm surf}, T, R_{\rm p}, a$	$p_{\rm surf}$, T , $R_{\rm p}$, a	$p_{\rm surf}, T, R_{\rm p}, a$
	No Constraint	$f_{\rm N_2}, f_{{\rm CO}_2}, M_{\rm p}, au_{\rm c}, f_{\rm c}$	$f_{\rm N_2}, f_{{\rm CO}_2}, M_{\rm p}, au_{\rm c}, f_{\rm c}$	$f_{\rm N_2}, f_{{\rm CO}_2}, M_{\rm p}, \tau_{\rm c}, f_{\rm c}$
Visible	Limited	$f_{\text{CH}_4}, p_c, \Delta p_c, \alpha$	$f_{\mathrm{CH_4}}, p_{\mathrm{c}}, \Delta p_{\mathrm{c}}, \alpha$	f_{CH_4} , Δp_c , α
$\lambda = [0.45 - 1.00] \mu \text{m}$	Weak Detection	f_{O_2} , T , A_{surf} , R_p , a	f_{O_2} , T , A_{surf} , R_p , a	T , A_{surf} , R_{p} , p_{c} , a
[0.10 -100] }	Detection	$f_{ m H_2O}, p_{ m surf}$	$p_{ m surf}$	
	Constraint	f_{O_3}	$f_{\rm H_2O},f_{\rm O_3}$	$f_{O_2}, f_{H_2O}, f_{O_3}, p_{surf}$
	No Constraint	$f_{\rm N_2}, f_{\rm O_2}, f_{\rm O_3}, A_{\rm surf}, M_{\rm p}$	$f_{\rm N_2}, f_{\rm O_2}, f_{\rm O_3}, A_{\rm surf}, M_{\rm p}$	$f_{\rm N_2},f_{\rm O_2},f_{\rm O_3},A_{\rm surf},M_{\rm p}$
NIR	Limited	$f_{\text{H}_2\text{O}}$, f_{CO_2} , f_{CH_4} , Δp_c , α	$f_{\rm H_2O}$, $f_{\rm CO_2}$, $f_{\rm CH_4}$, $\Delta p_{\rm c}$, α	$f_{\rm H_2O}$, $f_{\rm CO_2}$, $f_{\rm CH_4}$, $\Delta p_{\rm c}$, α
$\lambda = [1.00 - 1.80] \mu \text{m}$	Weak Detection	$p_{\mathrm{surf}}, R_{\mathrm{p}}, p_{\mathrm{c}}, \tau_{\mathrm{c}}, f_{\mathrm{c}}, a$	p_{surf} , R_{p} , p_{c} , τ_{c} , f_{c} , a	$p_{\rm surf}, R_{\rm p}, f_{\rm c}, a$
	Detection	T		p_{c}
	Constraint		T	$T, au_{ m c}$
	No Constraint	$f_{ m N_2},M_{ m p},a$	$f_{ m N_2},M_{ m p},a$	$f_{ m N_2},M_{ m p},a$
vNIR	Limited	$f_{\rm CO_2}$, $f_{\rm CH_4}$, $A_{\rm surf}$, $\Delta p_{\rm c}$, α	$f_{\rm CO_2}, f_{\rm CH_4}, A_{\rm surf}, \Delta p_{\rm c}, \alpha$	$f_{\rm CO_2}$, $f_{\rm CH_4}$, $A_{\rm surf}$, $\Delta p_{\rm c}$, α
$\lambda = [0.45 - 1.80] \mu \text{m}$	Weak Detection	$f_{\mathrm{O}_2},R_{\mathrm{p}},f_{\mathrm{c}}$	$R_{ m p},f_{ m c}$	$R_{ m p}$
. [Detection	$f_{\mathrm{H_{2}O}}, p_{\mathrm{surf}}, T, p_{\mathrm{c}}$	$p_{ m surf}$	
	Constraint	$f_{\mathrm{O_3}}, au_{\mathrm{c}}$	$f_{\rm O_2}, f_{\rm H_2O}, f_{\rm O_3}, T, p_{\rm c}, \tau_{\rm c}$	$f_{\rm O_2},f_{\rm H_2O},f_{\rm O_3},p_{\rm surf},T,p_{\rm c},\tau_{\rm c},f_{\rm c}$

Table 5. Detection Capabilities as a Function of the Spectral Coverage and S/N

4.4. Implications for Future Observatory Architectures

Our finding that wider spectral coverage plays a more decisive role than higher S/N in constraining key atmospheric and surface properties has important implications for the design of future direct imaging missions such as HWO.

First, extended wavelength coverage—particularly into the NIR—is essential for inferring cloud properties and atmospheric temperature. However, an exo-Earth target is more likely to fall within the coronagraph's inner working angle (IWA) at longer wavelengths, limiting access to features at these wavelengths for planets at small angular separations. Accessing the full NIR range therefore requires minimizing the IWA and/or increasing the telescope

aperture. A larger aperture not only improves angular resolution but also enhances photon collection, providing secondary benefits for S/N and overall characterization efficiency.

Second, by emphasizing the importance of broad spectral coverage, our results highlight the value of coronagraph designs that support wide instantaneous bandpasses or enable simultaneous observations across different spectral regions. This capability could be achieved through single multi-channel instruments or multiple instruments operating in parallel.

Taken together, these results support the development of mission architectures that:

- 1. minimize the coronagraph's IWA to enable full access to the visible and NIR ranges at relevant angular separations:
- 2. maximize the instrument bandpass width or enable multi-band parallel observations;
- 3. prioritize moderate-S/N observations across broad wavelength ranges over high-S/N spectroscopy in narrow bands.

Such designs would maximize the scientific return of early spectral observations of Earth analogs in unconstrained orbits, enabling robust atmospheric characterization even before orbit determination.

5. CONCLUSION

The most efficient observing strategies for searching for habitable Earth-analogs observed in reflected light with future space-based telescopes have yet to be fully defined. In this work, we explored how spectral coverage—particularly in coronagraph-restricted bandpasses—and the quality of direct imaging observations affect the ability to identify atmospheric and bulk properties of rocky exoplanets, assuming spectral observations are taken "early" (i.e., before any prior orbit measurements).

Using our atmospheric retrieval tool rfast, we evaluated the inference of 17 key atmospheric and planetary parameters for HWO-like observations covering various spectral bandpasses and spectral qualities ranging from moderate (S/N = 10) to moderate-high (S/N = 20). We deduced the observation requirements, in terms of spectral bandpass and quality (S/N), needed to infer this broad range of atmospheric and bulk exoplanet properties, and reciprocally assessed the detection capabilities of the tested observation scenarios. Our key findings are:

- Atmospheric composition cannot be reliably retrieved from a single Red or combined Blue & Red coronagraph-restricted bandpasses;
- Constraints on H₂O, O₂, and O₃ require observations spanning at least the Visible range, which also provides the best constraints on surface pressure;
- Cloud fraction, optical depth, and cloud-top pressure can be detected in the NIR;
- Observations combining Visible and NIR provide the best constraints for key atmospheric species abundances (H₂O, O₂, and O₃), cloud properties (cloud fraction, optical depth, and cloud-top pressure), surface pressure, and atmospheric temperature;
- Without prior knowledge, planet radius is systematically overestimated;
- Early spectral observations in unconstrained orbits can still robustly constrain the planet's thermo-chemical environment if spanning the Visible and NIR;
- A "spectrum first" approach could efficiently guide target prioritization and reduce repeated photometric observations of low-priority worlds;
- The choice of spectral bandpass is more critical than increasing S/N for retrieving atmospheric and surface properties and maximizing scientific return.

Overall, our results indicate that future direct imaging missions targeting Earth-analog characterization (such as the Habitable Worlds Observatory) could prioritize observations spanning broad spectral coverage, including the visible and possibly extending to the NIR, even at moderate S/N (10), rather than focusing on higher quality observations

confined to narrow coronagraph bandpasses. For example, a single coronagraph-restricted channel centered on a water absorption band can only place lower limits on water vapor abundance and is insufficient for detection, even at S/N = 20 combined with a Blue bandpass. In contrast, vNIR observations enable comprehensive constraints on the thermochemical state of the atmosphere through the inference of atmospheric composition, surface conditions, and cloud properties from moderate spectral quality data (S/N = 10). This approach not only maximizes the characterization potential from early observations in unconstrained orbits but also informs efficient mission planning and target selection, ultimately enhancing the search for habitable Earth-analogs.

ACKNOWLEDGMENTS

A.S. and T.D.R. gratefully acknowledge support from NASA's Habitable Worlds Program (No. 80NSSC20K0226) and NASA's Nexus for Exoplanet System Science Virtual Planetary Laboratory (No. 80NSSC18K0829). T.D.R. and A.S. also acknowledge support from the Cottrell Scholar Program administered by the Research Corporation for Science Advancement. A.S. warmly thanks the Bibliothèque Universitaire du Campus Périgord (Université de Bordeaux) and its team members, particularly Marie-Christine Emery-Bonnet, Catherine Dupin, and Nathalie Vidal, for providing office space and offering their welcoming support. A.S. is also grateful to Moina Issoufi for her invaluable assistance with figure design. Both authors thank an anonymous reviewer for their insightful and constructive comments.

Software: Astropy (Astropy Collaboration et al. 2013, 2018, 2022), corner (Foreman-Mackey 2016), emcee (Foreman-Mackey et al. 2013), matplotlib (Hunter 2007), NumPy (Harris et al. 2020), pandas (The pandas development team 2020), rfast (Robinson & Salvador 2023), seaborn (Waskom 2021)

APPENDIX

A. SIGNAL-TO-NOISE RATIO AS A FUNCTION OF WAVELENGTH

To inform mission design and planning tools—such as coronagraph exposure time and yield calculators—and facilitate integration of our results, we provide the signal-to-noise ratio (S/N) as a function of wavelength for each spectral coverage region considered (Table 2).

Three values of S/N_{λ_0} (10, 15, and 20) are considered to represent different spectral quality scenarios (Table 2). We define S/N_{λ_0} as the S/N set at the lower bound of each spectral coverage, denoted λ_0 . The corresponding noise level, computed at λ_0 for a given S/N_{λ_0} , is kept constant and propagated across the full bandpass (i.e., the noise is wavelength-independent). As a result, the S/N varies with wavelength and decreases within absorption features, where the reflected flux is lower (e.g., Feng et al. 2018; Robinson & Salvador 2023; Salvador et al. 2024).

Figure 8 illustrates how the specified values $S/N_{\lambda_0} = 10$, 15, and 20 translate to S/N at any other wavelength for each spectral coverage. For each color-coded spectral coverage and associated y-axis, the left, oblique, and right ticks correspond to $S/N_{\lambda_0} = 10$, 15, and 20, respectively, allowing direct estimation of the S/N at any wavelength within the bandpass.

As an example, in the continuum near the 0.94 μ m water absorption feature, e.g., at $\lambda = 0.87 \,\mu$ m, S/N_{0.87 μ m} is approximately 6.5 and 13 for the vNIR spectral coverage (green) when S/N_{$\lambda_0 = 0.45 \,\mu$ m} = 10 and 20, respectively. The same values apply to the Visible spectral coverage (yellow), which shares the same λ_0 .

This enables estimation of the local S/N at specific spectral regions of interest, which is particularly relevant for determining the exposure time required by coronagraphs targeting key molecular features within relatively narrow bandpasses.

B. RETRIEVAL RESULTS

Retrieval results obtained from observations conducted across the different spectral bandpasses are provided in:

- Table 6 for S/N = 10;
- Table 7 for S/N = 15;
- Table 8 for S/N = 20.

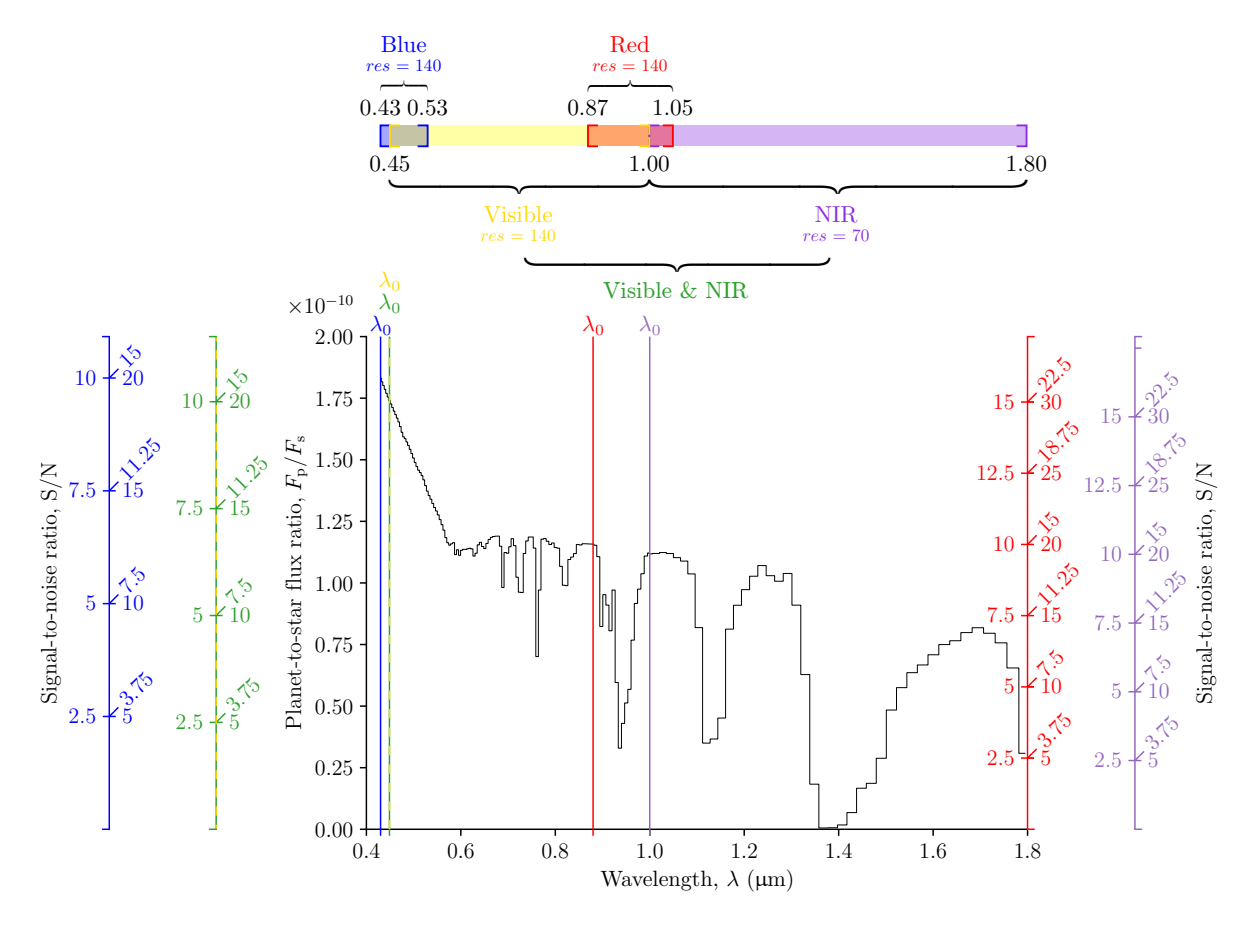


Figure 8. Reflected light spectrum of the fiducial case (black curve; see Figure 2 and Table 1) and corresponding signal-to-noise ratio (S/N; colored y-axes) as a function of wavelength for each color-coded spectral coverage (Table 2). The left, oblique, and right ticks of each colored y-axis correspond to $S/N_{\lambda_0} = 10$, 15, and 20, respectively, where λ_0 (indicated by vertical lines) is the lower bound of each spectral coverage at which the specified S/N_{λ_0} is defined. See text to extract the S/N at any wavelength of interest.

The Earth-based input values and the level of constraint for each parameter are also indicated (see subsection 3.1 for the inference classification). Corner plots showing the marginal univariate (along the diagonal) and joint bivariate (off-diagonal) posterior distributions of all retrieved parameters are provided in:

- Figure 9 for observations in the Visible bandpass at S/N = 10;
- Figure 10 for observations in the NIR bandpass at S/N = 20.

REFERENCES

Akeson, R., Armus, L., Bachelet, E., et al. 2019, arXiv, doi: 10.48550/arXiv.1902.05569 Alei, E., Konrad, B. S., Angerhausen, D., et al. 2022, Astronomy & Astrophysics, 665, A106, doi: 10.1051/0004-6361/202243760 Alei, E., Quanz, S. P., Konrad, B. S., et al. 2024,

Astronomy & Astrophysics, 689, A245, doi: 10.1051/0004-6361/202450320

Astropy Collaboration, Robitaille, T. P., Tollerud, E. J., et al. 2013, A&A, 558, A33, doi: 10.1051/0004-6361/201322068

Astropy Collaboration, Price-Whelan, A. M., Sipőcz, B. M., et al. 2018, AJ, 156, 123, doi: 10.3847/1538-3881/aabc4f

Astropy Collaboration, Price-Whelan, A. M., Lim, P. L., et al. 2022, ApJ, 935, 167, doi: 10.3847/1538-4357/ac7c74

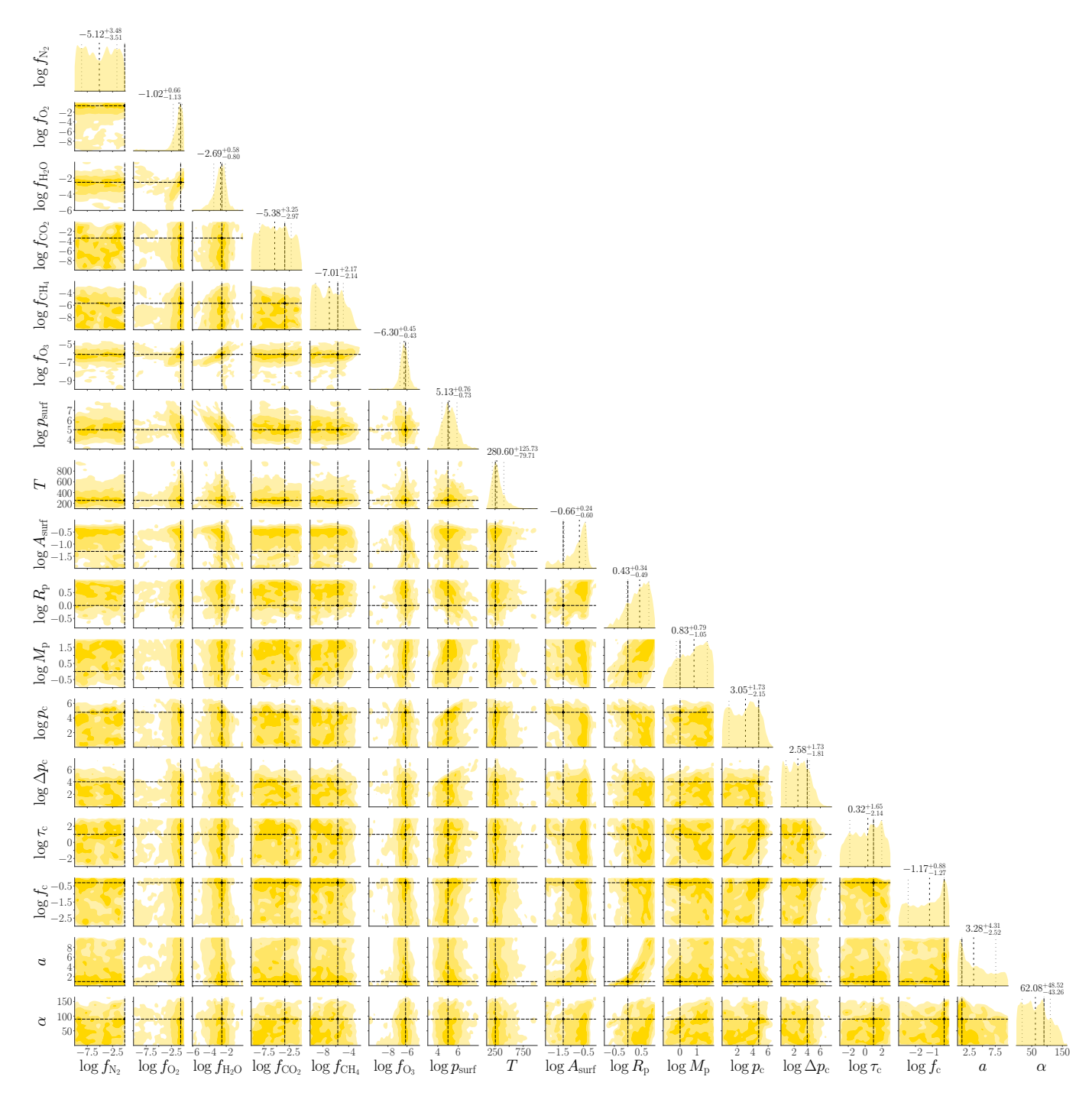


Figure 9. Corner plot showing the marginal univariate (along the diagonal) and joint bivariate (off-diagonal) posterior distributions of all 17 retrieved parameters from observations conducted in the Visible bandpass at S/N = 10. The retrieved values (loosely dashed) and their $\pm 1\sigma$ (68%) credible intervals (loosely dotted) are indicated by vertical lines on the 1D marginal distributions (i.e., the $16^{\rm th}$, $50^{\rm th}$, and $84^{\rm th}$ percentiles). The contours of the 2D posterior distributions correspond to the 1σ , 2σ , and 3σ levels, which encompass 68%, 95%, and 99.7% of the observed values, respectively. Note that these levels correspond to 39.3%, 86.5%, and 98.9% of the volume in 2D distributions, and to 68%, 95%, and 99.7% in 1D distributions. The vertical and horizontal dashed lines indicate the Earth-based input values.

 $\textbf{Table 6.} \ \ \text{Retrieval Results Comparison and Associated Level of Constraint for Observations Conducted in Different Spectral Coverages at S/N = 10$

Parameter	Input	Red	Blue & Red	Visible	NIR	vNIR
$\log f_{\mathrm{N}_2}$	-0.11	$-4.54^{+3.34}_{-3.62}$ NC	$-4.75^{+3.20}_{-3.50}$ NC	$-5.12^{+3.48}_{-3.51}$ NC	$-5.38^{+3.46}_{-3.10}$ NC	$-4.97^{+3.18}_{-3.50}$ NC
$\log f_{\mathrm{O}_2}$	-0.68	$-5.3 ^{+3.38}_{-3.41} \text{ NC}$	$-4.94^{+3.20}_{-3.42}$ NC	$-1.02^{+0.66}_{-1.13}$ WD	$-4.99^{+3.47}_{-3.22}$ NC	$-1.02^{+0.59}_{-0.89}$ WD
$\log f_{ m H_2O}$	-2.52	$-1.94^{+1.13}_{-1.59}$ L	$-2.12^{+1.17}_{-1.17}$ L	$-2.69^{+0.58}_{-0.80}$ D	$-1.73^{+1.11}_{-1.39}$ L	$-2.6^{+0.65}_{-0.55}$ D
$\log f_{\mathrm{CO}_2}$	-3.4	$-5.49^{+3.28}_{-3.26}$ NC	$-4.45^{+2.89}_{-3.77}$ NC	$-5.38^{+3.25}_{-2.97}$ NC	$-5.73^{+2.84}_{-2.93}$ L	$-6.1 ^{+2.90}_{-2.57}$ L
$\log f_{\mathrm{CH_4}}$	-5.7	$-6.83^{+2.42}_{-2.18}$ L	$-6.65^{+2.33}_{-2.27}$ L	$-7.01^{+2.17}_{-2.14}$ L	$-7.39^{+2.07}_{-1.80}$ L	$-7.42^{+1.82}_{-1.76}$ L
$\log f_{\mathrm{O_3}}$	-6.15	$-6.13^{+2.92}_{-2.71}$ NC	$-7.18^{+1.11}_{-1.83}$ L	$-6.3^{~+0.45}_{~-0.43}$ C	$-5.9 ^{+2.56}_{-2.77} NC$	$-6.26^{+0.42}_{-0.31}$ C
$\log p_{ m surf}$	5.0	$4.88^{+1.44}_{-0.94} \text{ WD}$	$4.8^{+1.25}_{-1.11}$ WD	$5.13^{+0.76}_{-0.73}$ D	$5.13^{+1.43}_{-1.06} \text{ WD}$	$5.28^{+0.70}_{-0.70}$ D
T	255.0	$277.09^{+95.47}_{-66.23}$ WD	$324.76^{+186.54}_{-116.35}$ WD	$280.6^{+125.73}_{-79.71}$ WD	$249.71^{+63.87}_{-58.48}$ D	262.43 ^{+64.32} _{-55.46} D
$\log A_{\mathrm{surf}}$	-1.3	$-0.62^{+0.44}_{-0.73}$ NC	$-0.89^{+0.40}_{-0.66}$ L	$-0.66^{+0.24}_{-0.60}$ WD	$-1.08^{+0.62}_{-0.59}$ NC	$-1.17^{+0.47}_{-0.55}$ L
$\log R_{\rm p}$	0.0	$0.44^{+0.35}_{-0.51} \text{ WD}$	$0.49^{+0.32}_{-0.47}$ WD	$0.43^{+0.34}_{-0.49}$ WD	$0.41^{+0.33}_{-0.59} \text{ WD}$	$0.5^{+0.26}_{-0.45} \text{ WD}$
$\log M_{ m p}$	0.0	$0.82^{+0.84}_{-1.06}$ NC	$0.8^{+0.80}_{-1.07}$ NC	$0.83^{+0.79}_{-1.05}$ NC	$0.92^{+0.77}_{-1.12}$ NC	$0.95^{+0.71}_{-1.00}$ NC
$\log p_{ m c}$	4.78	$2.79^{+1.65}_{-1.83}$ L	$2.56^{+1.74}_{-1.76}$ L	$3.05^{+1.73}_{-2.15}$ L	$4.44^{+0.89}_{-0.94} \text{ WD}$	$4.75^{+0.55}_{-0.58}$ D
$\log \Delta p_{ m c}$	4.0	$2.52^{+1.63}_{-1.68}$ L	$2.33^{+1.89}_{-1.68}$ L	$2.58^{+1.73}_{-1.81}$ L	$2.36^{+1.84}_{-1.68}$ L	$2.55^{+1.93}_{-1.84}$ L
$\log au_{ m c}$	1.0	$-0.07^{+1.95}_{-1.99}$ NC	$0.44^{+1.69}_{-2.13}$ NC	$0.32^{+1.65}_{-2.14}$ NC	$1.19^{+1.09}_{-0.34} \text{ WD}$	$1.05^{+0.49}_{-0.22}$ C
$\log f_{ m c}$	-0.3	$-1.32^{+1.04}_{-1.19}$ NC	$-1.38^{+0.93}_{-1.06}$ NC	$-1.17^{+0.88}_{-1.27}$ NC	$-0.27^{+0.22}_{-0.44} \text{ WD}$	$-0.32^{+0.24}_{-0.40} \text{ WD}$
a	1.0	$3.34^{+3.83}_{-2.37}$ NC	$2.95^{+3.53}_{-2.07}$ WD	$3.28^{+4.31}_{-2.52}$ WD	$2.74^{+3.94}_{-1.98} \text{ WD}$	$3.84^{+3.46}_{-2.78}$ NC
α	90.0	$65.79^{+47.86}_{-42.59} \mathrm{NC}$	$57.5 ^{+53.47}_{-45.14}$ L	$62.08^{+48.52}_{-43.26}$ L	$68.37^{+59.77}_{-46.54}$ L	$67.34^{+42.43}_{-44.39}$ L

 $\textbf{Table 7.} \ \ \text{Retrieval Results Comparison and Associated Level of Constraint for Observations Conducted in Different Spectral Coverages at S/N = 15$

Donomoton	Innut	Red	Blue & Red	Visible	NIR.	vNIR
Parameter	Input	neu	blue & neu	Visible	NIA	VIVIA
$\log f_{\mathrm{N}_2}$	-0.11	$-5.14^{+3.53}_{-3.30}$ NC	$-3.61^{+2.53}_{-4.47}$ NC	$-4.74^{+3.07}_{-3.62}$ NC	$-4.96^{+3.37}_{-3.17}$ NC	$-4.81^{+3.22}_{-3.35}$ NC
$\log f_{\mathrm{O}_2}$	-0.68	$-4.67^{+2.97}_{-3.38}$ NC	$-4.7 ^{+3.02}_{-3.38}$ NC	$-0.77^{+0.46}_{-0.57} \text{ WD}$	$-4.33^{+3.25}_{-3.94}$ NC	$-0.76^{+0.41}_{-0.52}$ C
$\log f_{ m H_2O}$	-2.52	$-1.68^{+0.94}_{-1.05}$ L	$-1.7^{~+0.83}_{~-0.91}$ L	$-2.58^{+0.46}_{-0.51}$ C	$-1.79^{+1.10}_{-1.05}$ L	$-2.55^{+0.47}_{-0.45}$ C
$\log f_{\mathrm{CO}_2}$	-3.4	$-5.45^{+3.56}_{-3.17}$ NC	$-5.03^{+3.36}_{-3.46}$ NC	$-5.4 ^{+3.07}_{-3.42} \text{ NC}$	$-5.92^{+2.70}_{-2.81}$ L	$-5.83^{+2.38}_{-2.88}$ L
$\log f_{\mathrm{CH_4}}$	-5.7	$-6.68^{+2.52}_{-2.36}$ L	$-6.81^{+2.64}_{-2.21}$ L	$-7.23^{+2.34}_{-1.85}$ L	$-7.49^{+2.02}_{-1.61}$ L	$-7.24^{+1.70}_{-1.82}$ L
$\log f_{\mathrm{O_3}}$	-6.15	$-6.22^{+2.67}_{-2.51}$ NC	$-7.15^{+1.09}_{-1.99}$ L	$-6.17^{+0.32}_{-0.32}$ C	$-5.82^{+2.33}_{-2.83}$ NC	$-6.2 ^{~+0.36}_{~-0.30}$ C
$\log p_{ m surf}$	5.0	$4.75^{+0.77}_{-0.71} \text{ WD}$	$4.63^{+0.95}_{-0.77}$ WD	$5.02^{+0.55}_{-0.52}$ D	$5.12^{+1.26}_{-0.88} \text{ WD}$	$5.17^{+0.56}_{-0.46}$ D
T	255.0	251.43 ^{+64.57} _{-44.11} D	$281.82^{+107.55}_{-74.27}$ WD	$269.03^{+75.16}_{-58.94}$ WD	$241.97^{+39.22}_{-35.48}$ C	$256.76^{+37.68}_{-34.37}$ C
$\log A_{ m surf}$	-1.3	$-0.69^{+0.47}_{-0.73}$ NC	$-1.07^{+0.45}_{-0.52}$ L	$-0.68^{+0.24}_{-0.50} \text{ WD}$	$-1.06^{+0.65}_{-0.65}$ NC	$-1.22^{+0.44}_{-0.46}$ L
$\log R_{\rm p}$	0.0	$0.39^{+0.37}_{-0.50} \text{ WD}$	$0.36^{+0.36}_{-0.42}$ WD	$0.39^{+0.32}_{-0.36} \text{ WD}$	$0.33^{+0.39}_{-0.50} \text{ WD}$	$0.48^{+0.30}_{-0.45} \text{ WD}$
$\log M_{ m p}$	0.0	$0.9^{+0.78}_{-1.02}$ NC	$0.92^{+0.77}_{-0.94}$ NC	$0.78^{+0.83}_{-1.01}$ NC	$0.92^{+0.74}_{-0.98}$ NC	$0.92^{+0.71}_{-1.05}$ NC
$\log p_{ m c}$	4.78	$3.01^{+1.46}_{-2.11}$ L	$2.65^{+1.69}_{-1.82}$ L	$3.15^{+1.59}_{-2.05}$ L	$4.52^{+0.68}_{-0.72} \text{ WD}$	$4.8 ^{~+0.41}_{~-0.41}$ C
$\log \Delta p_{ m c}$	4.0	$2.48^{+1.61}_{-1.66}$ L	$2.25^{+1.63}_{-1.49}$ L	$2.58^{+1.75}_{-1.70}$ L	$2.45^{+1.69}_{-1.70}$ L	$2.65^{+1.63}_{-1.74}$ L
$\log au_{ m c}$	1.0	$0.58^{+1.52}_{-2.29}$ NC	$-0.04^{+1.71}_{-2.05}$ NC	$0.21^{+1.54}_{-2.09}$ NC	$1.08^{+0.96}_{-0.22} \text{ WD}$	$1.01^{+0.33}_{-0.16}$ C
$\log f_{ m c}$	-0.3	$-1.16^{+1.02}_{-1.27}$ NC	$-1.41^{+0.99}_{-1.05}$ NC	$-1.21^{+0.92}_{-1.17}$ NC	$-0.23^{+0.17}_{-0.38} \text{ WD}$	$-0.31^{+0.21}_{-0.36} \text{ WD}$
a	1.0	$3.02^{+3.79}_{-2.19}$ NC	$1.62^{+2.56}_{-1.04}$ WD	$2.6^{+3.47}_{-1.75} \text{ WD}$	$2.28^{+3.50}_{-1.61} \text{ WD}$	$3.68^{+3.71}_{-2.53}$ NC
α	90.0	54.88 ^{+60.46} _{-36.92} L	$60.01^{+57.13}_{-40.02}$ L	$66.97^{+49.47}_{-46.20}$ L	$77.03^{+54.85}_{-55.61}$ L	63.0 ^{+42.09} _{-44.11} L

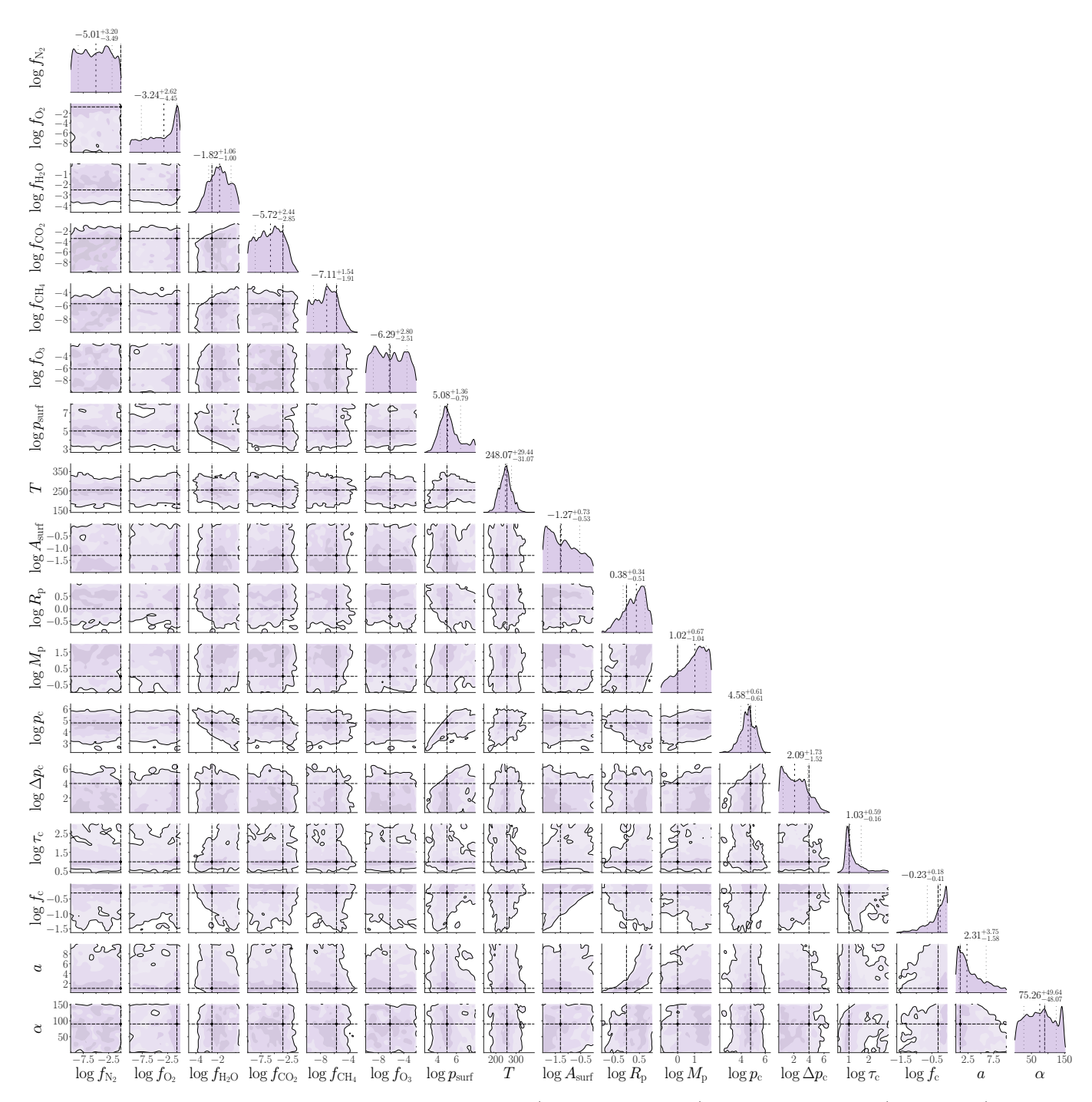


Figure 10. Corner plot showing the marginal univariate (along the diagonal) and joint bivariate (off-diagonal) posterior distributions of all 17 retrieved parameters from observations conducted in the NIR bandpass at S/N = 20. The retrieved values (loosely dashed) and their $\pm 1\sigma$ (68%) credible intervals (loosely dotted) are indicated by vertical lines on the 1D marginal distributions (i.e., the 16^{th} , 50^{th} , and 84^{th} percentiles). The contours of the 2D posterior distributions correspond to the 1σ , 2σ , and 3σ levels, which encompass 68%, 95%, and 99.7% of the observed values, respectively. Note that these levels correspond to 39.3%, 86.5%, and 98.9% of the volume in 2D distributions, and to 68%, 95%, and 99.7% in 1D distributions. The vertical and horizontal dashed lines indicate the Earth-based input values.

 $\textbf{Table 8.} \ \ \text{Retrieval Results Comparison and Associated Level of Constraint for Observations Conducted in Different Spectral Coverages at S/N = 20$

Parameter	Input	Red	Blue & Red	Visible	NIR	vNIR
$\log f_{\mathrm{N}_2}$	-0.11	$-4.43^{+2.85}_{-3.71}$ NC	$-4.93^{+3.49}_{-3.26}$ NC	$-4.7 ^{\ +3.06}_{\ -3.43} \ \mathrm{NC}$	$-5.01^{+3.20}_{-3.49}$ NC	$-5.1 ^{+3.28}_{-3.47} \text{ NC}$
$\log f_{\mathrm{O}_2}$	-0.68	$-4.85^{+3.14}_{-3.71}$ NC	$-4.95^{+3.07}_{-3.30}$ NC	$-0.68^{+0.38}_{-0.42}$ C	$-3.24^{+2.62}_{-4.45}$ NC	$-0.77^{+0.35}_{-0.40}$ C
$\log f_{\mathrm{H_2O}}$	-2.52	$-1.56^{+0.98}_{-0.97}$ L	$-1.67^{+0.88}_{-0.98}$ L	$-2.52^{+0.40}_{-0.45}$ C	$-1.82^{+1.06}_{-1.00}$ L	$-2.57^{+0.38}_{-0.41}$ C
$\log f_{\mathrm{CO}_2}$	-3.4	$-5.38^{+3.30}_{-2.96}$ NC	$-5.15^{+3.11}_{-3.26}$ NC	$-5.04^{+3.15}_{-3.24}$ NC	$-5.72^{+2.44}_{-2.85}$ L	$-6.53^{+2.47}_{-2.38}$ L
$\log f_{\mathrm{CH_4}}$	-5.7	$-6.71^{+2.20}_{-2.28}$ L	$-6.5 ^{+2.16}_{-2.32}$ L	$-6.8 ^{+2.28}_{-2.03}$ L	$-7.11^{+1.54}_{-1.91}$ L	$-7.44^{+1.70}_{-1.74}$ L
$\log f_{\mathrm{O}_3}$	-6.15	$-6.11^{+2.88}_{-2.46}$ NC	$-6.78^{+0.89}_{-2.14}$ L	$-6.13^{+0.31}_{-0.28}$ C	$-6.29^{+2.80}_{-2.51}$ NC	$-6.22^{+0.30}_{-0.25}$ C
$\log p_{\mathrm{surf}}$	5.0	$4.72^{+0.66}_{-0.65}$ NC	$4.6^{+0.83}_{-0.76}$ NC	$5.01^{+0.47}_{-0.42}$ C	$5.08^{+1.36}_{-0.79}$ NC	$5.16^{+0.55}_{-0.41}$ C
T	255.0	$255.83^{+41.90}_{-39.19}$ C	$257.27^{+69.80}_{-52.79}$ WD	$263.67^{+53.22}_{-40.87}$ WD	$248.07^{+29.44}_{-31.07}$ C	$254.56^{+31.44}_{-27.08}$ C
$\log A_{ m surf}$	-1.3	$-0.67^{+0.48}_{-0.88}$ NC	$-1.17^{+0.49}_{-0.50}$ L	$-0.76^{+0.32}_{-0.63} \text{ WD}$	$-1.27^{+0.73}_{-0.53}$ NC	$-1.28^{+0.38}_{-0.46}$ L
$\log R_{ m p}$	0.0	$0.28^{+0.43}_{-0.41} \text{ WD}$	$0.4_{-0.35}^{+0.31} \text{ WD}$	$0.33^{+0.30}_{-0.35} \text{ WD}$	$0.38^{+0.34}_{-0.51} \text{ WD}$	$0.47^{+0.28}_{-0.47} \text{ WD}$
$\log M_{ m p}$	0.0	$0.95^{+0.75}_{-1.10}$ NC	$0.97^{+0.75}_{-1.07}$ NC	$0.66^{+0.83}_{-0.90}$ NC	$1.02^{+0.67}_{-1.04}$ NC	$0.8 ^{+0.75}_{-1.00} \ \mathrm{NC}$
$\log p_{ m c}$	4.78	$3.37^{+1.16}_{-2.21}$ L	$3.13^{+1.55}_{-2.00}$ L	$4.3^{+0.65}_{-1.80} \text{ WD}$	$4.58^{+0.61}_{-0.61}$ D	$4.81^{+0.34}_{-0.33}$ C
$\log \Delta p_{ m c}$	4.0	$2.13^{+1.60}_{-1.42}$ L	$1.99^{+1.73}_{-1.28}$ L	$2.27^{+1.79}_{-1.62}$ L	$2.09^{+1.73}_{-1.52}$ L	$2.33^{+1.74}_{-1.56}$ L
$\log au_{ m c}$	1.0	$0.53^{+1.48}_{-2.30}$ NC	$0.36^{+1.49}_{-2.00}$ NC	$0.67^{+1.27}_{-2.01}$ NC	$1.03^{+0.59}_{-0.16}$ C	$1.0 ^{~+0.23}_{~-0.12}$ C
$\log f_{ m c}$	-0.3	$-1.12^{+0.99}_{-1.31}$ NC	$-1.26^{+1.00}_{-1.14}$ NC	$-0.95^{+0.72}_{-1.34}$ NC	$-0.23^{+0.18}_{-0.41} \text{ WD}$	$-0.26^{+0.19}_{-0.29}$ C
a	1.0	$2.06^{+3.40}_{-1.41} \text{ WD}$	$1.73^{+1.84}_{-1.03} \text{ WD}$	$2.24^{+2.45}_{-1.47} \text{ WD}$	$2.31^{+3.75}_{-1.58}$ WD	$3.68^{+3.63}_{-2.47}$ NC
α	90.0	$73.43^{+54.62}_{-49.44}$ L	$62.75^{+57.70}_{-46.09}$ L	$70.88^{+52.92}_{-49.12}$ L	$75.26^{+49.64}_{-48.07}$ L	$66.28^{+37.97}_{-45.75}$ L

- Bailey, V. P., Bottom, M., Cady, E., et al. 2018, in Space Telescopes and Instrumentation 2018: Optical, Infrared, and Millimeter Wave, ed. M. Lystrup, H. A. MacEwen, G. G. Fazio, N. Batalha, N. Siegler, & E. C. Tong, Vol. 10698, International Society for Optics and Photonics (SPIE), 106986P, doi: 10.1117/12.2313820
- Barstow, J. K. 2020, Monthly Notices of the Royal Astronomical Society, 497, 4183, doi: 10.1093/mnras/staa2219
- Barstow, J. K., & Heng, K. 2020, Space Science Reviews, 216, 82, doi: 10.1007/s11214-020-00666-x
- Benneke, B., & Seager, S. 2012, The Astrophysical Journal, 753, 100, doi: 10.1088/0004-637X/753/2/100
- Carrión-González, Ó., García Muñoz, A., Cabrera, J., et al. 2020, Astronomy & Astrophysics, 640, A136, doi: 10.1051/0004-6361/202038101
- Carrión-González, Ó., García Muñoz, A., Santos, N. C., et al. 2021, Astronomy & Astrophysics, 655, A92, doi: 10.1051/0004-6361/202141469
- Corrales, L., Gavilan, L., Teal, D. J., & Kempton, E. M.-R. 2023, The Astrophysical Journal Letters, 943, L26, doi: 10.3847/2041-8213/acaf86
- Currie, M. H., & Meadows, V. S. 2025, The Planetary Science Journal, 6, 96, doi: 10.3847/PSJ/adc004
- Currie, M. H., Meadows, V. S., & Rasmussen, K. C. 2023, The Planetary Science Journal, 4, 83, doi: 10.3847/PSJ/accf86
- Damiano, M., Burr, Z., Hu, R., Burt, J., & Kataria, T.
 2025, The Astronomical Journal, 169, 97,
 doi: 10.3847/1538-3881/ada610
- Damiano, M., & Hu, R. 2020, The Astronomical Journal, 159, 175, doi: 10.3847/1538-3881/ab79a5
- —. 2022, The Astronomical Journal, 163, 299, doi: 10.3847/1538-3881/ac6b97
- Damiano, M., Hu, R., & Hildebrandt, S. R. 2020, The Astronomical Journal, 160, 206, doi: 10.3847/1538-3881/abb76a
- Damiano, M., Hu, R., & Mennesson, B. 2023, The Astronomical Journal, 166, 157, doi: 10.3847/1538-3881/acefd3
- Fauchez, T. J., Turbet, M., Villanueva, G. L., et al. 2019,
 The Astrophysical Journal, 887, 194,
 doi: 10.3847/1538-4357/ab5862
- Feng, Y. K., Robinson, T. D., Fortney, J. J., et al. 2018, The Astronomical Journal, 155, 200, doi: 10.3847/1538-3881/aab95c
- Foreman-Mackey, D. 2016, The Journal of Open Source Software, 1, 24, doi: 10.21105/joss.00024

- Foreman-Mackey, D., Hogg, D. W., Lang, D., & Goodman, J. 2013, Publications of the Astronomical Society of the Pacific, 125, 306, doi: 10.1086/670067
- Fortney, J. J., Barstow, J. K., & Madhusudhan, N. 2021, in ExoFrontiers, 2514-3433 (IOP Publishing), 10–17, doi: 10.1088/2514-3433/abfa8fch17
- Fujii, Y., & Matsuo, T. 2021, The Astronomical Journal, 161, 180, doi: 10.3847/1538-3881/abe129
- Gaudi, B. S., Seager, S., Mennesson, B., et al. 2018, Nature Astronomy, 2, 600, doi: 10.1038/s41550-018-0549-2
- —. 2020, arXiv e-prints, doi: 10.48550/arXiv.2001.06683
- Gialluca, M. T., Robinson, T. D., Rugheimer, S., & Wunderlich, F. 2021, Publications of the Astronomical Society of the Pacific, 133, 54401, doi: 10.1088/1538-3873/abf367
- Gilbert-Janizek, S., Meadows, V. S., & Lustig-Yaeger, J. 2024, The Planetary Science Journal, 5, 148, doi: 10.3847/PSJ/ad381e
- Greene, T. P., Line, M. R., Montero, C., et al. 2016, The Astrophysical Journal, 817, 17, doi: 10.3847/0004-637X/817/1/17
- Guimond, C. M., & Cowan, N. B. 2019, The Astronomical Journal, 157, 188, doi: 10.3847/1538-3881/ab0f2e
- Guyon, O., Pluzhnik, E. A., Kuchner, M. J., Collins, B., & Ridgway, S. T. 2006, The Astrophysical Journal Supplement Series, 167, 81, doi: 10.1086/507630
- Hall, S., Krissansen-Totton, J., Robinson, T., Salvador, A., & Fortney, J. J. 2023, The Astronomical Journal, 166, 254, doi: 10.3847/1538-3881/ad03e9
- Harris, C. R., Millman, K. J., van der Walt, S. J., et al. 2020, Nature, 585, 357, doi: 10.1038/s41586-020-2649-2
- Horak, H. G., & Little, S. J. 1965, The Astrophysical Journal Supplement Series, 11, 373, doi: 10.1086/190119
- Hunter, J. D. 2007, Computing in Science & Engineering, 9, 90, doi: 10.1109/MCSE.2007.55
- Kasdin, N. J., Bailey, V., Mennesson, B., et al. 2020, in Space Telescopes and Instrumentation 2020: Optical, Infrared, and Millimeter Wave, ed. M. Lystrup,
 N. Batalha, E. C. Tong, N. Siegler, & M. D. Perrin, Vol. 11443, International Society for Optics and Photonics (SPIE), 194, doi: 10.1117/12.2562997
- Kasting, J. F., Whitmire, D. P., & Reynolds, R. T. 1993, Icarus, 101, 108, doi: 10.1006/icar.1993.1010
- Kawashima, Y., & Rugheimer, S. 2019, The Astronomical Journal, 157, 213, doi: 10.3847/1538-3881/ab14e3
- Kelkar, S., Saxena, P., Kopparapu, R., & Monteiro, J. 2025, The Planetary Science Journal, 6, 87, doi: 10.3847/PSJ/adbe7f

- Kofman, V., Villanueva, G. L., Fauchez, T. J., et al. 2024, The Planetary Science Journal, 5, 197, doi: 10.3847/PSJ/ad6448
- Komacek, T. D., Fauchez, T. J., Wolf, E. T., & Abbot,
 D. S. 2020, The Astrophysical Journal Letters, 888, L20,
 doi: 10.3847/2041-8213/ab6200
- Konrad, B. S., Alei, E., Quanz, S. P., et al. 2022, Astronomy & Astrophysics, 664, A23, doi: 10.1051/0004-6361/202141964
- Kopparapu, R. K., Ramirez, R., Kasting, J. F., et al. 2013, Astrophysical Journal, 770, doi: 10.1088/0004-637X/770/1/82
- Latouf, N., Himes, M. D., Mandell, A. M., et al. 2024, The Astronomical Journal, 169, 50,

doi: 10.3847/1538-3881/ad9729

- Latouf, N., Mandell, A. M., Villanueva, G. L., et al. 2023a, The Astronomical Journal, 166, 129, doi: 10.3847/1538-3881/acebc3
- —. 2023b, The Astronomical Journal, 167, 27, doi: 10.3847/1538-3881/ad0fde
- Lupu, R. E., Marley, M. S., Lewis, N., et al. 2016, The Astronomical Journal, 152, 217, doi: 10.3847/0004-6256/152/6/217
- Lustig-Yaeger, J., Meadows, V. S., Crisp, D., Line, M. R., & Robinson, T. D. 2023, Planetary Science Journal, 4, 170, doi: 10.3847/PSJ/acf3e5
- Lustig-Yaeger, J., Stevenson, K. B., Mayorga, L. C., et al. 2021, The Astrophysical Journal Letters, 921, L4, doi: 10.3847/2041-8213/ac2cc2
- Madhusudhan, N. 2018, in Handbook of Exoplanets, ed. H. J. Deeg & J. A. Belmonte (Cham: Springer International Publishing), 2153–2182, doi: 10.1007/978-3-319-55333-7_104
- Mai, C., & Line, M. R. 2019, The Astrophysical Journal, 883, 144, doi: 10.3847/1538-4357/ab3e6d
- Mandell, A. M., Lustig-Yaeger, J., Stevenson, K. B., & Staguhn, J. 2022, The Astronomical Journal, 164, 176, doi: 10.3847/1538-3881/ac83a5
- Marley, M., Lupu, R., Lewis, N., et al. 2014, arXiv e-prints, doi: 10.48550/arXiv.1412.8440
- Meadows, V. S., Lincowski, A. P., & Lustig-Yaeger, J. 2023, The Planetary Science Journal, 4, 192, doi: 10.3847/PSJ/acf488
- Mennesson, B., Juanola-Parramon, R., Nemati, B., et al. 2020, arXiv, doi: 10.48550/arXiv.2008.05624

- Mennesson, B., Bailey, V. P., Zellem, R., et al. 2022, in Space Telescopes and Instrumentation 2022: Optical, Infrared, and Millimeter Wave, ed. L. E. Coyle,
 S. Matsuura, & M. D. Perrin, Vol. 12180, International Society for Optics and Photonics (SPIE), 121801W, doi: 10.1117/12.2629176
- Mennesson, B., Belikov, R., Por, E., et al. 2024, Journal of Astronomical Telescopes, Instruments, and Systems, 10, 35004, doi: 10.1117/1.JATIS.10.3.035004
- Mettler, J.-N., Konrad, B. S., Quanz, S. P., & Helled, R.
 2024, The Astrophysical Journal, 963, 24,
 doi: 10.3847/1538-4357/ad198b
- Metz, C. O., Kiang, N. Y., Villanueva, G. L., Parenteau, M. N., & Kofman, V. 2024, The Planetary Science Journal, 5, 228, doi: 10.3847/PSJ/ad769d
- Min, M., Ormel, C. W., Chubb, K., Helling, C., & Kawashima, Y. 2020, Astronomy & Astrophysics, 642, A28, doi: 10.1051/0004-6361/201937377
- Morgan, R., Savransky, D., Turmon, M., et al. 2022, in Space Telescopes and Instrumentation 2022: Optical, Infrared, and Millimeter Wave, ed. L. E. Coyle,
 S. Matsuura, & M. D. Perrin, Vol. 12180, International Society for Optics and Photonics (SPIE), 1218020, doi: 10.1117/12.2630609
- Morgan, R., Savransky, D., Turmon, M., et al. 2024, in Space Telescopes and Instrumentation 2024: Optical, Infrared, and Millimeter Wave, ed. L. E. Coyle,
 S. Matsuura, & M. D. Perrin, Vol. 13092, International Society for Optics and Photonics (SPIE), 130925M, doi: 10.1117/12.3020858
- National Academies of Sciences, Engineering, and Medicine. 2021, Pathways to Discovery in Astronomy and Astrophysics for the 2020s (Washington, DC: The National Academies Press), doi: 10.17226/26141
- —. 2022, Origins, Worlds, and Life: A Decadal Strategy for Planetary Science and Astrobiology 2023-2032 (Washington, DC: The National Academies Press), doi: 10.17226/26522
- Nayak, M., Lupu, R., Marley, M. S., et al. 2017,Publications of the Astronomical Society of the Pacific,129, 034401, doi: 10.1088/1538-3873/129/973/034401
- Novais, A., Fisher, C., Ghezzi, L., et al. 2025, Monthly Notices of the Royal Astronomical Society, staf397, doi: 10.1093/mnras/staf397
- Pidhorodetska, D., Fauchez, T. J., Villanueva, G. L., Domagal-Goldman, S. D., & Kopparapu, R. K. 2020, The Astrophysical Journal Letters, 898, L33, doi: 10.3847/2041-8213/aba4a1
- Plavchan, P., Latham, D., Gaudi, S., et al. 2015, arXiv e-prints, doi: 10.48550/arXiv.1503.01770

- Rauer, H., Aerts, C., Cabrera, J., & Team, P. 2016, Astronomische Nachrichten, 337, 961, doi: 10.1002/asna.201612408
- Rauer, H., Catala, C., Aerts, C., et al. 2014, Experimental Astronomy, 38, 249, doi: 10.1007/s10686-014-9383-4
- Rauer, H., Aerts, C., Cabrera, J., et al. 2024, The PLATO Mission, doi: 10.48550/arXiv.2406.05447
- Roberge, A., & Moustakas, L. A. 2018, Nature Astronomy, 2, 605, doi: 10.1038/s41550-018-0543-8
- Robinson, T. D., & Salvador, A. 2023, The Planetary Science Journal, 4, 10, doi: 10.3847/PSJ/acac9a
- Robinson, T. D., Meadows, V. S., Crisp, D., et al. 2011, Astrobiology, 11, 393, doi: 10.1089/ast.2011.0642
- Salvador, A., Robinson, T. D., Fortney, J. J., & Marley, M. S. 2024, The Astrophysical Journal Letters, 969, L22, doi: 10.3847/2041-8213/ad54c5
- Seager, S., & Deming, D. 2010, Annual Review of Astronomy and Astrophysics, 48, 631, doi: 10.1146/annurev-astro-081309-130837
- Shaklan, S., Lisman, D., McKeithen, D., et al. 2024, in Space Telescopes and Instrumentation 2024: Optical, Infrared, and Millimeter Wave, ed. L. E. Coyle,
 S. Matsuura, & M. D. Perrin, Vol. 13092, International Society for Optics and Photonics (SPIE), 130925D, doi: 10.1117/12.3020798
- Shaklan, S., McKeithen, D., Lisman, D., & Dumont, P. 2023, in Techniques and Instrumentation for Detection of Exoplanets XI, ed. G. J. Ruane, Vol. 12680, International Society for Optics and Photonics (SPIE), 1268010, doi: 10.1117/12.2677793
- Smith, A. J. R. W., Feng, Y. K., Fortney, J. J., et al. 2020, The Astronomical Journal, 159, 36, doi: 10.3847/1538-3881/ab5a8a

- Stark, C. C., Dressing, C., Dulz, S., et al. 2020, The Astronomical Journal, 159, 286, doi: 10.3847/1538-3881/ab8f26
- Stark, C. C., Latouf, N., Mandell, A. M., & Young, A. 2024, Journal of Astronomical Telescopes, Instruments, and Systems, 10, 14005, doi: 10.1117/1.JATIS.10.1.014005
- Stark, C. C., Belikov, R., Bolcar, M. R., et al. 2019, Journal of Astronomical Telescopes, Instruments, and Systems, 5, 24009, doi: 10.1117/1.JATIS.5.2.024009
- Stevenson, K. B. 2020, The Astrophysical Journal Letters, 898, L35, doi: 10.3847/2041-8213/aba68c
- Susemiehl, N., Mandell, A. M., Villanueva, G. L., et al. 2023, The Astronomical Journal, 166, 86, doi: 10.3847/1538-3881/ace43b
- The LUVOIR Team. 2019, arXiv e-prints, doi: 10.48550/arXiv.1912.06219
- The pandas development team. 2020, pandas-dev/pandas: Pandas, v1.5.3, Zenodo, doi: 10.5281/zenodo.3509134
- Tokadjian, A., Hu, R., & Damiano, M. 2024, The Astronomical Journal, 168, 292, doi: 10.3847/1538-3881/ad88eb
- von Paris, P., Hedelt, P., Selsis, F., Schreier, F., & Trautmann, T. 2013, Astronomy & Astrophysics, 551, A120, doi: 10.1051/0004-6361/201220009
- Wang, F., Fujii, Y., & He, J. 2022, The Astrophysical Journal, 931, 48, doi: 10.3847/1538-4357/ac67e5
- Wang, J., Mawet, D., Hu, R., et al. 2018, Journal of Astronomical Telescopes, Instruments, and Systems, 4, 35001, doi: 10.1117/1.JATIS.4.3.035001
- Waskom, M. L. 2021, Journal of Open Source Software, 6, 3021, doi: 10.21105/joss.03021
- Welbanks, L., & Madhusudhan, N. 2019, The Astronomical Journal, 157, 206, doi: 10.3847/1538-3881/ab14de
- Young, A. V., Crouse, J., Arney, G., et al. 2024, The Planetary Science Journal, 5, 7, doi: 10.3847/PSJ/ad09b1